ELECTROCHEMICAL STUDY OF UNDER-POTENTIAL DEPOSITION PROCESSES ON TRANSITION METAL SURFACES

Sarah Cecilia Flores Araujo, B.S.

Thesis Prepared for the Degree of

MASTER OF SCIENCE

UNIVERSITY OF NORTH TEXAS

August 2006

APPROVED:

Oliver M.R. Chyan, Major Professor
Teresa D. Golden, Committee Member
Ruthanne D. Thomas, Chair of the
    Department of Chemistry
Sandra L. Terrell, Dean of the Robert B.
    Toulouse School of Graduate Studies

Flores Araujo, Sarah Cecilia, Electrochemical Study of Under-Potential Deposition Processes on Transition Metal Surfaces, Master of Science (Chemistry), August 2006, 121 pp., 4 tables, 41 figures, reference list, 115 references.

Copper under-potential deposition (UPD) on iridium was studied due to important implications it presents to the semiconductor industry. Copper UPD allows controlled superfilling on sub-micrometer trenches; iridium has characteristics to prevent copper interconnect penetration into the surrounding dielectric. Copper UPD is not favored on iridium oxides but data shows copper over-potential deposition when lower oxidation state Ir oxide is formed.

Effect of anions in solution on silver UPD at platinum (Pt) electrodes was studied with the electrochemical quartz crystal microbalance. Silver UPD forms about one monolayer in the three different electrolytes employed. When phosphoric acid is used, silver oxide growth is identified due to presence of low coverage hydrous oxide species at potentials prior to the monolayer oxide region oxide region.

ACKNOWLEDGEMENTS

My profound appreciation and acknowledgements are to all the people who helped me in accomplishing this very important goal. Thanks to Dr. Oliver M.R. Chyan whose support was essential in the continuation of my studies, and whose advice and knowledge was fundamental for my academic development. My unique acknowledgements are for Dr. Teresa Golden, from whom I obtained invaluable knowledge, support and understanding. The financial support from the UNT Faculty Research Grant and the Welch Foundation is to a great extent appreciated, as well as the help from the UNT Chemistry Department staff. Special thanks to the members of my group, Praveen Nalla, Yibin Zhang, Shyam Venkataraman, Kai-Hung Yu, and Karthikeyan Pillai, whose enthusiasm and discussions helped in the accomplishment of the work presented here.

I would like to extend my acknowledgements to Dr. Oscar Mendoza, whose guide and help was essential for the arrival to UNT. To Dr. Rosa Amelia Orozco, Dr. Manuel Quevedo, and Dr. Alejandro Hernández, whose unconditional friendship I truly appreciate. Exceptional acknowledgements to my family and my in-laws whose confident love, values, support and friendship is invaluable, making me withstand the most difficult situations; and to Oscar Ojeda, whose love, support and confidence made it possible.

TABLE OF CONTENTS

Chapters

3 EFFECT OF DIFFERENT ELECTROLYTES ON SILVER UNDER-POTENTIAL DEPOSITION AT PLATINUM EQCM 67

LIST OF TABLES

Page

LIST OF FIGURES

CHAPTER 1

INTRODUCTION

1.1 Under-Potential Deposition of Metals

The under-potential deposition of metals is a phenomenon that has been subject of study in the past decades since 1970s, and it refers to the deposition of metals on a foreign metal substrate at potentials more positive than the predicted by the Nernst equation for the bulk deposition of metals [1-3].

In 1974, Kolb studied the chemisorption of metal atoms on metal surfaces in correlation to work function differences [2]. It was explained that the binding energy for the adsorbed atoms on the substrate exceeds the binding energy of the atoms in the respective bulk crystal, and later in the same year, electrolytic deposition of metal atoms onto foreign metal substrates at under-potential were studied in aqueous and non-aqueous solutions with the intention to express the fact that under-potential deposition is a general phenomenon under certain conditions that is even found at the solid-vacuum interface [3]. Studies that make use of electrochemical techniques confirm the generality of this phenomenon, since it has been observed that it is independent of concentration or scan rate, and that it depends on plane orientation of the foreign metal.

Bruckenstein and Swathirajan studied in 1983 the equilibrium dynamic properties of under-potential deposition on polycrystalline substrates with special emphasis on information obtained from the rotating disk electrode technique [4], and from there, extensive studies involving under-potential deposition of different metals on polycrystalline [5] and single crystal surfaces [6] have been made while using different electrochemical techniques.

For this study, the under-potential deposition of Cu and Ag are studied with the use of potential sweep methods (e.g. cyclic voltammetry, linear sweep voltammetry). These systems show a Nernstian behavior and results can be analyzed by making use of the concepts that will be described in the following sections.

1.2 Fundamental Concepts of Electrochemistry

In order to obtain the data that would allow the analysis of the under-potential deposition of Cu and Ag, a conventional three-way electrode cell was employed. In this arrangement the current is passed between the electrode of interest or working electrode (WE) and a counter electrode (CE), and the potential of the WE is monitored relative to a separate reference electrode (RE) that has the characteristic of approaching ideal nonpolarizability [7].

For a chemical process in solution, the free energy (ΔG) associated with the transfer of an electron to an oxidized species in solution is seen to be composed of the free energy associated with transfer of the oxidized species from solution to vacuum, the free energy associated with the transfer of an electron to the oxidized species in vacuum, and the free energy associated with the transfer of the reduced species from vacuum to solution [8]. If the oxidized and reduced species are at unit activity then the free energy of the reduction is a standard free energy and has the usual relationship to the standard reduction potential:

$$\Delta G^{\circ} = -nFE^{\circ} \qquad (1)$$

The standard potential E° is an empirical constant expressing the redox-active energy levels on the oxidized and reduced species in the general process:

$$O + ne \Leftrightarrow R \qquad (2)$$

For this process in equilibrium condition [7], thermodynamic arguments show that the Nernst Equation corresponds to:

$$E = E^{0} + \frac{RT}{nF} ln \frac{a_O}{a_R} \qquad (3)$$

Where a_O and a_R are the activities of the oxidized and reduced species. It is usually more convenient to work with concentrations instead of activities and hence the Nernst equation can be rewritten as follows:

$$E = E^{0} + \frac{RT}{nF} ln \frac{\gamma_O}{\gamma_R} + \frac{RT}{nF} ln \frac{C_O^*}{C_R^*} = E^{0}{}' + \frac{RT}{nF} ln \frac{C_O^*}{C_R^*} \qquad (4)$$

Where the $E^{\circ\prime}$ is the formal potential that includes the activity coefficients for the specific medium, and generally the difference between standard and formal potential is not expected to be great.

The Nernst equation provides a correlation between electrode potential E and the concentration of participants in the electrode process. If a system follows the Nernst equation or an equation derived from it, the electrode reaction is often said to be thermodynamically or electrochemically reversible (or Nernstian). It is important to emphasize that the Nernst equation is valid only at the equilibrium condition [13]. Electrochemical techniques like cyclic voltammetry involve non-equilibrium conditions, and therefore cannot be expected to exhibit a Nernstian response unless rates are very fast and equilibrium is quickly reestablished in the surface.

Cyclic voltammetry (CV) and linear sweep voltammetry (LSV) techniques were used in this study. These belong to the potential sweep methods in which, particularly CV, the potential is varied linearly with time at different sweep rates (v) in a reversible manner as shown in Fig 1-1. If swept to negative potentials, the species near the electrode are reduced, and when the potential is reversed after certain time λ or at the switching potential (E_λ), the species become reoxidized and the resulting currents are measured Fig 1-2. CV is one of the most effective electroanalytical techniques available for probing redox systems, and it has become very popular in electrochemistry to obtain information about quite complicated electrode reactions [13].

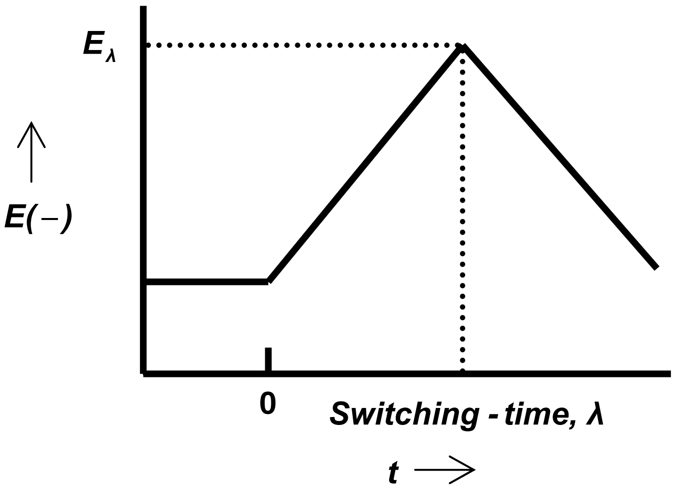

Figure 1-1 Cyclic potential sweep.

Two important parameters in CV are the peak potential (E_p) and the peak current (i_p), which are the potential and current at the characteristic voltammogram peak as shown in Fig 1-2, and from which important information can be obtained like formal potentials or peak to peak separations.

The formal redox potential ($E^{o\prime}$) for a reversible process can be obtained by the mean of the peak potentials:

$$E^{\circ\prime} = \frac{E_c + E_a}{2} \tag{5}$$

As mentioned, another important parameter is the separation of the peak potentials ΔE_p. The theoretical value for ΔE_p for a reversible process is $\frac{0.057}{n}$ V

[8]. However, the measured value for a reversible process is generally higher due to the presence of defects on the electrode surface, uncompensated solution resistance and non-linear diffusion, and a poor cleaning procedure of the surface.

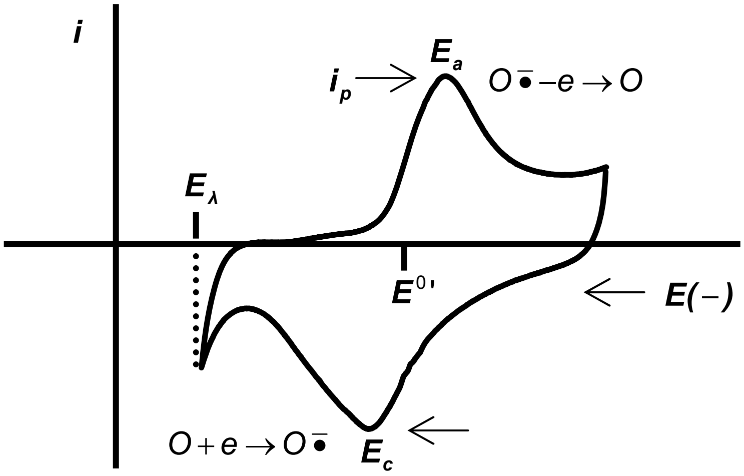

Figure 1-2 Resulting cyclic voltammogram.

For a reversible system the peak current is defined by the Randles-Sevcik equation,

$$i_p = (2.69x10^5)n^{3/2}AD^{1/2}Cv^{1/2} \tag{6}$$

Where i_p is the peak current (A), n is the number of electrons transferred, A is the electroactive area (cm^2), D the diffusion coefficient of the species being oxidized/reduced ($cm^2 \cdot s^{-1}$), C is the concentration of this same species in the bulk solution ($mol \cdot cm^{-3}$), and v is the scan rate ($V \cdot s^{-1}$). For this study, equation (6) can be used in order to determine the electroactive area of the electrode after the CV data has been obtained. The linear sweep voltammetry technique differs from CV in that it involves only one scan without a reverse one.

The potential sweep methods are controlled potential techniques where a potentiostat is essential to direct the electrical potential between the working and reference electrodes in a three-electrode cell at a preset value. The potentiostat forces whatever current is necessary to flow between the working and counter electrodes to keep the desired potential, as long as the needed cell voltage and current do not exceed the compliance limits of the potentiostat. In this study, the electrochemical experiments were performed using a CH Instruments ©[*] 400 or a 440 model time-resolved EQCM potentiostat, and controlled by a personal computer. The instrument's software was used to record all data from electrochemical experiments.

1.3 Electrode Preparation

The electrodes used for the electrochemical experiments corresponding to Chapter 2 were made with Ir ESPI[†] shots. Following is the step by step procedure on how to prepare an electrode, but for a more detailed description on

---

[*] CH Instruments, Inc. http://www.chinstruments.com

[†] Electronic Space Products Incorporated, http://www.espi-metals.com

the materials and polishing procedure, the reader can refer to the laboratory manual [38].

The mold where the metal shot is supported consists of the non-tapered end of an MLA pipette, which was cut off as shown in Figure 1-3.

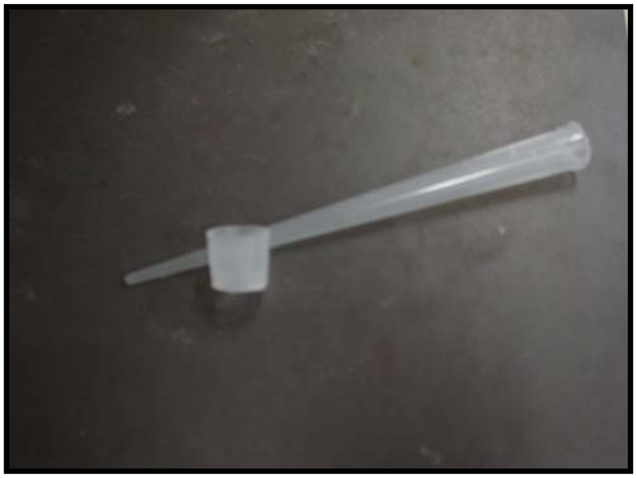

Figure 1-3 Non-tapered end of an MLA pipette as electrode mold.

By placing the metal shot on a clean and hard surface, a 6-inch copper wire is soldered to the metal shot as presented in Figure 1-4.

Then the mold is placed on a sheet of Parafilm ®[*] with the larger uncut opening facing down, and the soldered shot and wire in the center of the mold. As shown in Figure 1-5, a mixture of LECO™[†] epoxy is poured slowly into the mold and allowed to cure for 24 hours under a plastic or wooden box to minimize the effects of air currents.

---

[*] Pechiney Plastic Packaging, http://www.parafilm.com

[†] Leco Corporation, http://www.leco.com

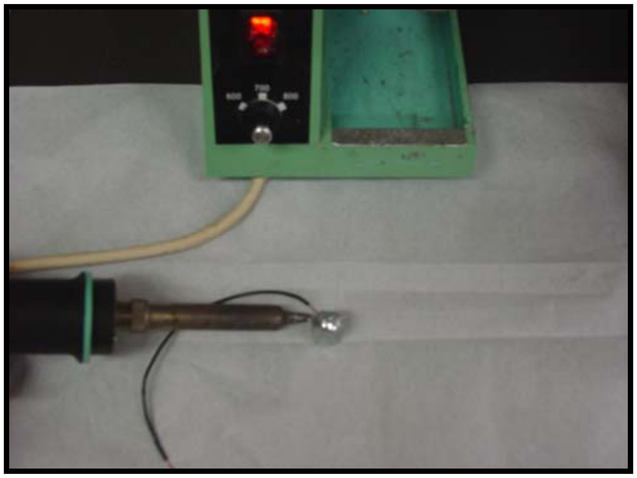

Figure 1-4 Soldering of the Cu wire to the Ir metal shot.

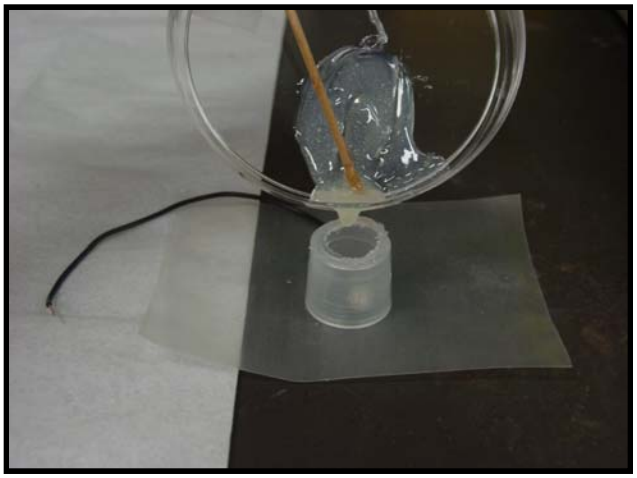

Figure 1-5 Soldered Ir metal shot in mold with epoxy.

When the epoxy has dried, the plastic mold is removed and the piece is ready to be placed in the lapping fixture as shown in Figure 1-6. The purpose of the lapping fixture is to achieve a completely flat surface during the polishing steps. The polishing procedure is probably the most time consuming part of the electrode preparation since a mirror finish is expected in order to have the desired surface to study electrochemical reactions.

Figure 1-6 Electrode fixed in lapping fixture ready for coarse grinding.

The electrode goes through a coarse grinding with the aid of a rotating wheel, where silicon carbide (SiC) polishing pads of different grit from Allied ©[*] are used in the following order: 60 grit, 180 grit, 320 grit, 600 grit, and 800 grit polishing pad. Following the coarse grinding, the fine grinding can be achieved without the aid of the lapping fixture as shown in Figure 1-7.

With 6μ and 1μ SiC polishing pads and the use of poly diamond suspensions from Allied®[†] the mirror finish can be achieved in the electrode as is shown by the microscope image from Figure 1-8.

---

[*] Allied, High Tech Products, Inc., http://www.alliedhightech.com

[†] Allied, High Tech Products, Inc., http://www.alliedhightech.com

Figure 1-7 Fine grinding without the aid of lapping fixture.

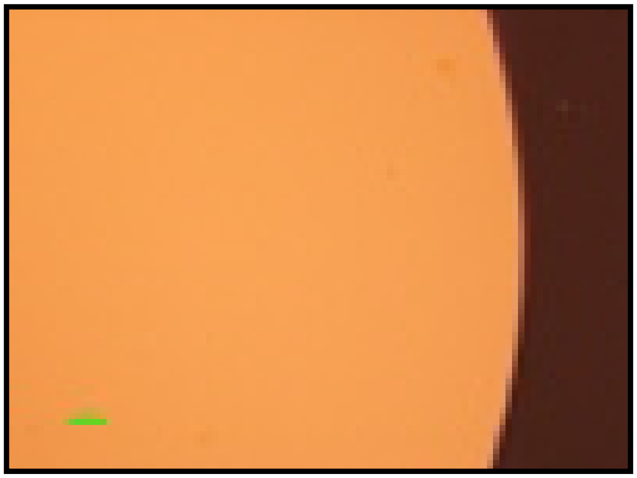

Figure 1-8 Microscope image of freshly polished electrode to mirror finish.

1.4 Electrochemical Quartz Crystal Microbalance

This sophisticated analytical technique is based on the quartz crystal microbalance (QCM) technology. As depicted in Figure 1-9, QCM comprises a thin quartz crystal sandwiched between two metal electrodes that establish an alternating electric field across the crystal, causing vibrational motion of the crystal at its resonant frequency [9-12]. This resonant frequency is sensitive to mass changes and other factors of the crystal and its electrodes.

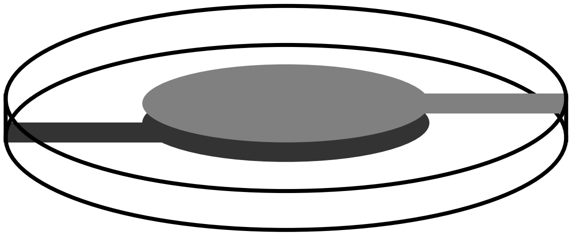

Figure 1-9 Thin quartz crystal sandwiched between two metal electrodes.

The electrochemical quartz crystal microbalance (EQCM), which is the electrochemical application of the QCM, has provided a powerful approach to examining electrochemical processes involving thin films, including monolayer and submonolayer films [16-18]. These studies have revealed detailed mechanistic information about film deposition and dissolution, surface morphology changes, and mass changes in thin films caused by redox or other chemical processes [14, 15].

In its earliest form, the EQCM was used in ex situ experiments to measure mass changes at electrode surfaces after electrodeposition of metals. Later, the experimental methods required for its use as an in situ mass sensor for thin films on electrode surfaces were developed so that mass changes and various other processes could be monitored in real-time.

1.4.1 Fundamentals of Operation

The EQCM is a piezoelectric device that employs alpha quartz crystals because of the superior mechanical and piezoelectric properties of this kind of quartz [11]. This piezoelectric quartz crystal resonator is a precisely cut wafer taken from a natural or synthetic single crystal of quartz like the one shown in Figure 1-10 [19].

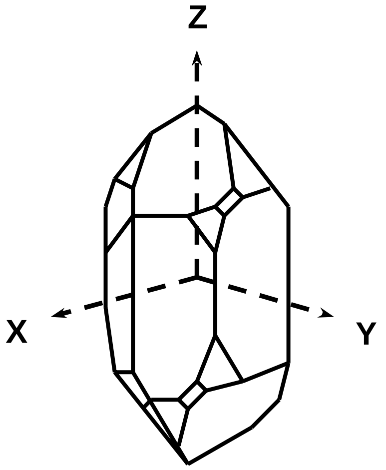

Figure 1-10 The perfect natural form of a quartz crystal.

Pierre and Jacques Curie discovered the phenomenon of piezoelectricity in 1880 in many substances including natural quartz. They observed that when pressure was applied to some crystals in particular directions, an electric potential was produced between the deformed surfaces of the crystal, with the potential being proportional to the applied pressure. This behavior is referred to as the piezoelectric effect, which is derived from the Greek word “piezein”, meaning to press. Only crystals without a center of symmetry possess this property [10].

The converse piezoelectric effect in which application of a voltage across these crystals resulted in a corresponding shear strain is the basis of the QCM. If an alternating potential is applied, vibrational motion occurs within the quartz crystal lattice. Stable oscillation can be attained only at the natural resonant frequency of the crystal, and at that frequency the crystal presents low impedance to the exciting voltage. This crystal is thus called a quartz resonator [10].

The useful mode of vibration in the QCM is the high frequency thickness-shear mode that indicates that the motion of the disk surface is precisely parallel to the disk face, and has been shown to be sensitive to the addition or removal of mass at the electrode surface.

This kind of vibration is shown in Figure 1-11 [12] for the fundamental mode where two major surfaces of such a resonator are always antinodal, with a node existing in the center of the wafer. The disk thickness and shear deformation have been exaggerated for clarity in the Figure. Typical frequencies for these oscillations in EQCMs are from 1 to 10 megahertz (MHz) [10-12].

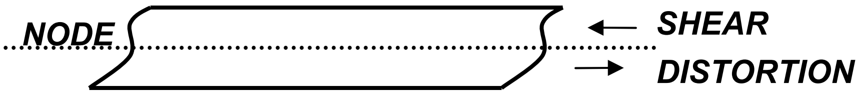

Figure 1-11 Edge view of QCM disk showing shear deformation.

In order for a quartz crystal to oscillate in the thickness-shear mode, the crystal must be cut at specific angles of orientation relative to the principal optical axis. Figure 1-12 [12] shows the two kind of cuts that are employed for QCM applications, the AT-cut with an angle of 35° 15’ (left), and the BT-cut (right), with an angle of 49° 00’.

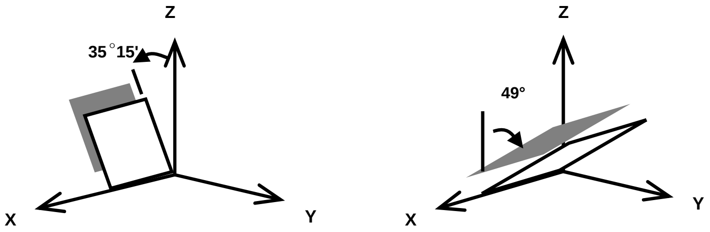

Figure 1-12 AT (left) and BT-cut (right) quartz crystal plates.

AT-cut crystals are particularly popular because they can minimize the effect of temperature on the frequency, and can be cut to give nearly zero temperature coefficients at one or two temperatures [12]. Therefore this kind of cut crystal is used in the present study.

1.4.2 Electrochemical Apparatus

Figure 1-9 [10] shows a QCM disk with vapor deposited electrodes in a keyhole pattern which are thin film Au, Pt or any other metal electrodes with a thickness of 1000 Å. A thin adhesion layer of either Cr or Ti is usually deposited directly onto the quartz crystal to aid in the adhesion of the metal electrode. Even if there are smaller QCMs, the most commonly used are 1-inch diameter and have a central circular pad of 0.280 cm^2; for this study the employed QCMs have a central circular pad of 0.205 cm^2. The “flag” has minimal influence on oscillator stability.

The QCM is mounted in an apparatus like the one in the schematic of Figure 1-13. Most of the methods for mounting make it possible to expose only one side of the EQCM disk to the electrolyte solution, which is the working electrode side. This is usually necessary to prevent the two EQCM electrodes from being capacitively shunted by the solution, which can cause the cessation of oscillation. Cells of chemically inert materials like Teflon®[*] can be employed to mount the EQCM sandwiched between two o-rings. In all cases, the cells should be designed so that the oscillator circuitry is situated as close as possible to the crystal to minimize the length of the leads from the circuit to the crystal. The oscillator circuit is connected to the frequency counter, which generates either an analog or digital signal for the computer acquisition system.

---

[*] Du Pont, http://www.teflon.com

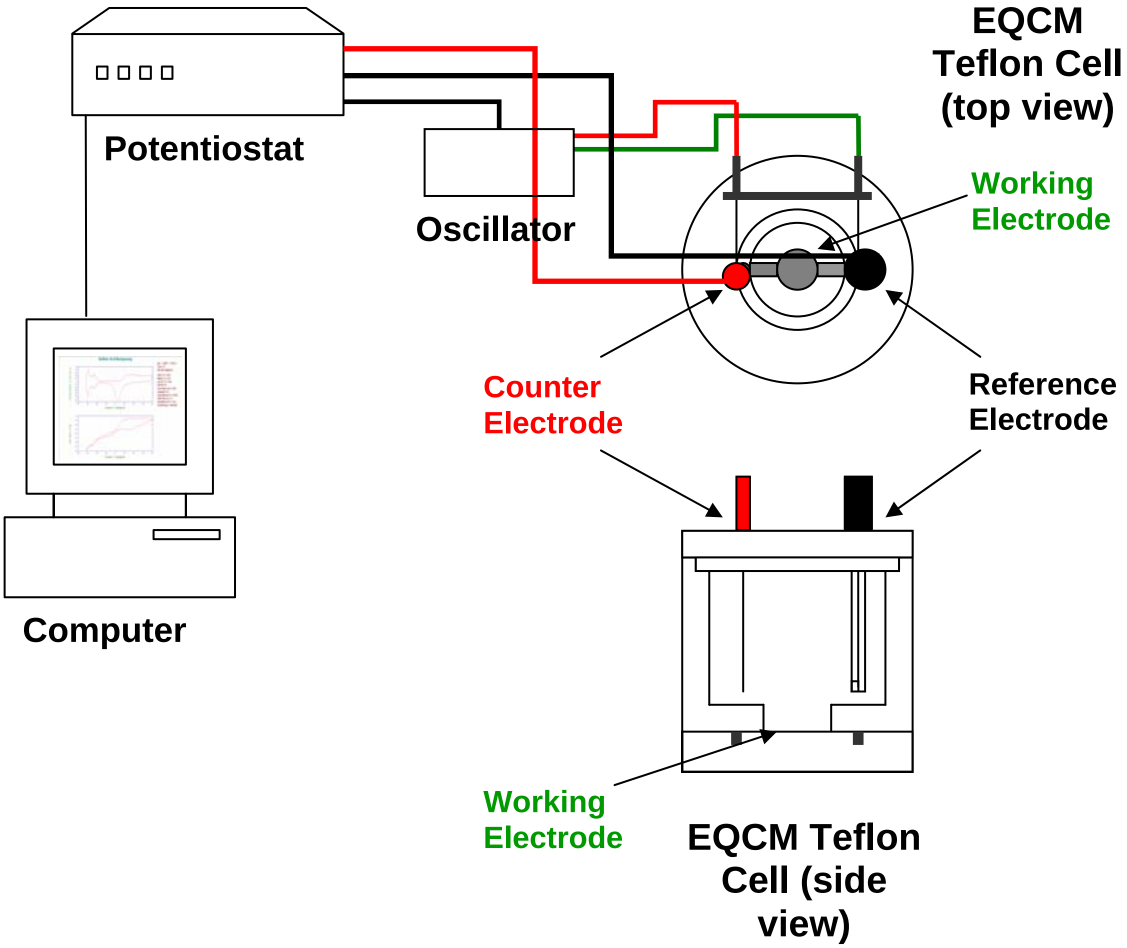

Figure 1-13 Electrochemical quartz crystal microbalance setup.

1.4.3 Frequency-Mass Correlations

As mentioned earlier, when a piezoelectric crystal resonator is used as a mass sensor, the mass change is inferred from the change of its resonant frequency. Thus, the relationship between the mass and frequency must be known quantitatively. Sauerbrey was the first to recognize the potential usefulness of AT and BT crystals as mass sensors. He demonstrated the extremely sensitive nature of these piezoelectric devices towards mass changes at the surface of the QCM electrodes. He also described their differential radial mass sensitivity and correlated this with the radial distribution of the vibrational amplitude. The results of his pioneering work in this area are embodied in the Sauerbrey equation, which relates the mass change per unit area at the QCM electrode surface to the observed change in oscillation frequency of the crystal:

$$\Delta f = -\left(\frac{2nf_0^2}{\left(\rho_q \mu_q\right)^{1/2}} \right) \Delta m \qquad (7)$$

Where Δf is the frequency change caused by addition of a mass per unit area, *m*, to the crystal surface, *n* is the harmonic number of the oscillation (e.g., *n* = 1 for 5 MHz with a 5 MHz crystal), μ is the shear modulus of quartz (2.95 x 10^{11} g·cm^{-1} ·s^{-2}), and ρ is the density of quartz (2.65 g·cm^{-3}). The constants are usually lumped together to yield a single constant, the sensitivity factor, C_f

$$\Delta f = -C_f \Delta m \qquad (8)$$

Which has the value of 1.42 x10^{-9} Hz·ng^{-1} for a 7.995 MHz crystal like the one employed in this study. As seen from Equation (7), the mass sensitivity is dependent of the square of resonant frequency (f_0). Higher frequency operation of the quartz crystal thus offers the advantage of grater mass sensitivity.

Although the Sauerbrey relationship was derived for QCM operation in gas phase, it is still applicable to the operation in liquids under appropriate conditions. Therefore the behavior of the QCM depends on the medium in which it is operating, because the medium couples to the crystal surface and affects the shear mode.

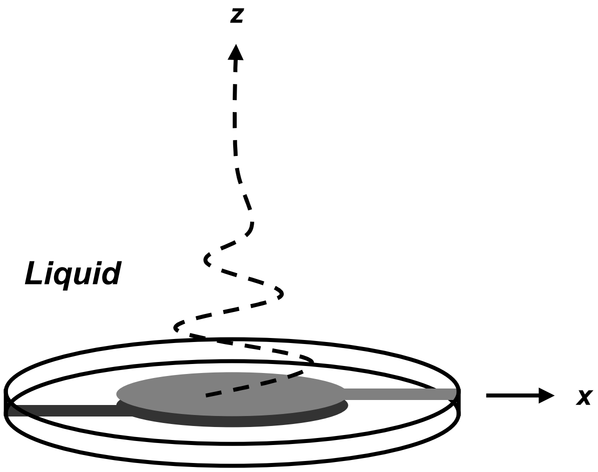

Figure 1-14 Propagation of the transverse shear wave from the QCM into a liquid.

When a planar surface that is oscillating in a shear mode is immersed into any medium, a shear wave propagates normally away from the surface into the medium in the form of acoustic waves as represented in Figure 1-14 [20]. This behavior was first treated by Glassford, and later by Kanazawa and Gordon. Kanazawa's treatment of the influence of the solution properties on the crystal permits the prediction of the change in resonant frequency that accompanies immersion of the crystal into a viscous medium:

$$\Delta f = -f_o^{3/2}\left(\frac{\rho_1\eta_1}{\pi\rho_q\mu_q}\right)^{1/2} \tag{9}$$

Where the decrease in resonant frequency is seen to be proportional to $(\rho_1\eta_1)^{1/2}$, the square root of the density times the viscosity of the medium. This equation predicts the decrease in frequency (f_0) of ca. 700 Hz on transfer from vacuum to pure water at 20°C [10, 12].

If the crystal is being used as the frequency determining element in a circuit, frequency's changes may be observed that are not derived from mass changes but rather result from some other factors, and a non-ideal behavior is suspected. Some of these factors are temperature, viscoelastic properties, surface roughness and porosity, and surface stress, which are fully described in the references [10, 12]. Detailed publications can be found that describe the possible and future applications of the EQCM as well as the main concerns regarding its use [21-30], and several attempts have been made to integrate it with a rotating device to obtain rotating EQCM data [34], or even incorporate it to scanning electrochemical microscopy to monitor film mass and surrounding electrolyte composition during potential cycling [35].

For some, the question that if the quartz crystal microbalance is really a mass sensor has been answered in a recent publication by Mecea [36] based on its description as an actuator that generates a mega-gravity, time-dependent inertial field on the surface of the quartz. The very high mass sensitivity of the quartz crystal microbalance is explained by the very high intensity of the field acting on the deposited film, and based on these ideas, three fundamental principles for mass measurements are formulated and demonstrated: the field principle, the mass sensitivity principle and the general equivalence principle.

1.5 X-Ray Photoelectron Spectroscopy

X-ray photoelectron spectroscopy (XPS), also known as electron spectroscopy for chemical analysis (ESCA), is an electron spectroscopy method commonly used to elucidate chemical and structural components of surfaces. It was developed in the mid 1960s by K. Siegban and his research group, and its principle of operation is based on the Photoelectric Effect where the concept of photon is used to describe the ejection of electrons from the atom’s core energy levels when a monochromatic electromagnetic wave impinge upon it, and overcomes its binding energy as shown in Figure 1-15.

The XPS employs soft rays like Al and Mg Kα (1486.6 eV and 1253.6 eV respectively) as photon energies of choice, and sometimes Ti Kα with energy of 2040 eV is used.

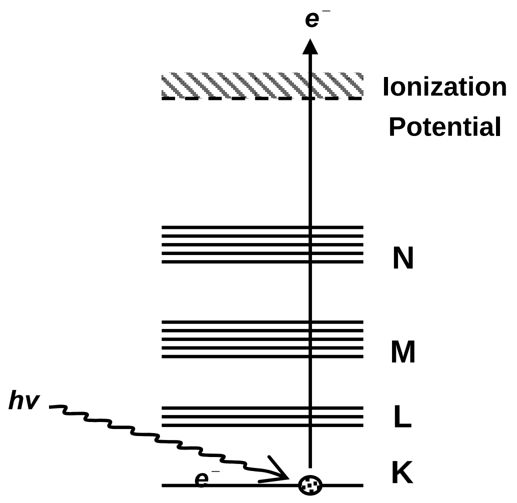

Figure 1-15 Principle of operation for XPS.

The XPS is highly surface specific due to the short range of the photoelectrons that are excited from the solid. The kinetic energy (E_{KE}) of these photoelectrons is determined by the energy of the x-ray radiation, hv, and the electron binding energy (E_{BE}) as follows:

$$E_{KE} = hv - E_{BE} \tag{10}$$

The experimentally measured energies of the photoelectrons are given by:

$$E_{KE} = hv - \Phi - E_{BE} \tag{11}$$

Where Φ is the work function of the spectrometer or analyzer.

The detected kinetic energy is related to the binding energy of the analyzed species by the used of the work function of the analyzer, and the energy of the monochromatic beam. The energy of the photoelectrons leaving the sample give a spectrum with a series of photoelectron peaks, and the binding energy of the peaks are characteristic of each element. The peak areas can be used to determine the composition of the material's surface, and the shape of each peak and the binding energy can be slightly altered by the chemical oxidation state of the emitting atom as well as by the electron affinity of the chemical environment where the photoelectron was emitted [37].

In the present study, the results from XPS analysis were obtained in a VG®[*] ESCALAB MK II spectrometer, with an Al Kα emission ray as source of excitation.

1.6 Conclusions

In this first chapter some of the fundamental concepts of electrochemistry that are relevant to this work were described together with the methodology used for the preparation of the working Ir electrode.

A detailed description of the electrochemical quartz crystal microbalance is included, as well as an explanation of its principle of operation based on frequency measurements that can be correlated to mass changes on the surface of the balance by the Sauerbrey equation. References can be found that explain in further detail the future applications of this powerful electrochemical

---

[*] Thermo Electron Corporation, http://www.thermo.com

instrument, as well as new literature that reveals exciting theory behind the quartz crystal technology.

Finally a concise explanation of the XPS technique is presented, which is one of the surface analysis techniques that provided surface characterization and confirmed some of the results in Chapter 2 of this study.

1.7 References

1. Gerisher, H.; Kolb, D.M.; Przasnyski, M.; *Surface Science* 1974, 43, 662-666.
2. Kolb, D.M., *Advances in Electrochemistry and Electrochemical Engineering,* 1978. John Wiley Interscience: New York. vol. 11. p. 125.
3. Kolb, D.M.; Przasnyski, M.; Gerisher, H.; *Electroanal. Chem. Interfac. Electrochem.* 1974, 54, 25-38.
4. Swathirajan, S.; Bruckenstein, S.; *Electrochim. Acta* 1983, 28(7), 865-877.
5. Van Huong C.N.; Gonzalez-Tejera, M.J.; *J. Electroanal. Chem.* 1988 244, 249-259.
6. Herrero, E.; Buller, L.J.; Abruña, H.D.; *Chem. Rev.* 2001, 101, 1897-1930.
7. Faulkner, L.R. Electrochemical *Characterization of Chemical Systems*. 1983. Academic Press, Inc.: vol. 3. p. 137.
8. Grosser, D.K., *Cyclic Voltammetry: Simulation and Analysis of Reaction Mechanism*. 1993, New York: Wiley-VCH.
9. Buttry D. A.; Ward, M. D. *Chem. Review,* 1992, *92,* 1355-1379.
10. Zhang, M., Ph. D. Thesis, University of Ottawa: Ottawa, Canada, 1995.

11. Salt, D. *Hy-Q Handbook of Quartz Crystal Devices,* Van Nostrand Reinhold: UK, 1987, pp 5-36, 160-162.
12. Buttry, D.A. *Applications of the Quartz Crystal Microbalance to Electrochemistry*, in *Electroanalytical Chemistry: A series of Advances*; Bard, A. J. Marcel Dekker: New York, 1996, pp 1-85.
13. Bard, A. J.; Faulkner, L. R. *Electrochemical Methods: Fundamentals and Applications*. Second Edition, John Wiley and Sons Inc.: New York, 2001, pp 725.
14. Aurbach, D.; Moshkovich, M. *J. Electrochem. Soc.* 1998, 145(8), 2629-2639.
15. Il-Hwan, K.; Kwang-Bum, K. *J. Electrochem. Soc.* 2004, 151(1), E7-E13.
16. Ostrom, G. S.; Buttry, D. A. *J. Phys. Chem.* 1995, 99(41), 15236-40.
17. Ariizumi, N.; Kamijo, M. *Yamanashi-ken Kogyo Gijutsu Senta Kenkyu Hokoku* 2000, 14, 12-17.
18. Sadik, O. A.; Cheung, M-C. *Talanta* 2001, 55(5), 929-941.
19. O'Sullivan, C.K.; Guilbault, G. G. *Biosensors & Bioelectronics* 1999, 14, 663-670.
20. Lee, W.; White, H. S.; Ward, M. D. *Anal. Chem.* 1993, 65, 3232-3237.
21. Deakin, M.R.; Buttry, D. A. *Anal. Chem.* 1989, 61(20), 1147A-1154A.
22. Wunsche, M. *Electrochim. Acta* 1995, 5(40), 629-635.
23. Kraznaric, G. *Langmuir* 2001, 17, 43-4351.
24. Lay et al. *J. Electroanal. Chem.* 2003, 1, 1-11.

25. Herrero, E.; Buller, L. J.; Abruña, H. D. *Chem. Rev.* 2001, 101(7), 1897-1930.
26. Nicic, L. et al. *J. Phys. Chem. B* 2002, 106, 12247-12252.
27. Uchida, H.; Hiei, M.; Watanabe, M. *J. Electroanal. Chem.* 1998, 452(1), 97-106.
28. Marx, K.A., et al. *Biosensors and Bioelectronics* 2001, 16, 773-782.
29. Tenreiro, A.; Cordas, C. M.; Abrantes, L. M. *Portugaliae Electrochim. Acta* 2003, 21(4), 361-370.
30. Jiang, M.; Ray, W. W.; Mukherjee, B.; Wang, J. *Electrochem. Comm.* 2004, 6, 576-582.
31. Ward, M.D.; Buttry, D.A.; *Science*, 1990, 249(4972), 1000-1007.
32. Deakin, M.R.; Buttry, D.A.; *Anal. Chem*. 1989, 61(20), 1147A-1154A.
33. Jeffrey, M.I.; Zheng, J.; Ritchie, I.M.; *Meas. Sci. Technol*. 2002, 11, 560-567.
34. Vergé, M.-G.; Mettraux, P.; Olsson, C.-O.A.; Landolt, D.; *J. Electroanal. Chem.* 2004, 566, 361-370.
35. Cliffel, D.E.; Bard, A.J.; *Anal. Chem*. 1998, 70, 1993-1998.
36. Mecea, V.M.; Sensors and Actuators A, 2006, 128, 270-277.
37. Nascente, P.A.P., *Journal of Molecular Catalysis A: Chemical*, 2005. 228: p. 145-150.
38. Flores, S. *Making an Electrode*, 2003.

CHAPTER 2

COPPER UNDER-POTENTIAL DEPOSITION ON IRIDIUM

2.1 Introduction

Copper under-potential deposition has been a subject of study in the past decades especially on platinum and gold substrates, and extensive studies with different analytical techniques have been made in order to understand this process [1-6 and references therein].

The competitive semiconductor industry is in constant technological development and search of new materials that can meet the nano scale conditions favorable for the miniaturization of on-chip interconnects. Therefore, copper under-potential deposition has been recently studied in substrates like ruthenium and its conductive ruthenium oxide due to the strong binding interaction that exists between copper and these two kinds of substrates [7]. Ultra thin films composed of ruthenium and its conductive oxides are promising candidates as a directly copper plateable diffusion barrier for future metal interconnects application, and copper under-potential deposition has important implications since it allows the controlled superfilling on sub-micrometer trenches [8].

Encouraged by these kinds of studies, copper deposition has been recently studied on iridium metal surfaces due to the characteristics iridium has to prevent penetration of copper interconnect material into the surrounding dielectric [9]; this supports the potential iridium has to substitute Ta/TaN barriers (Figure 2-1).

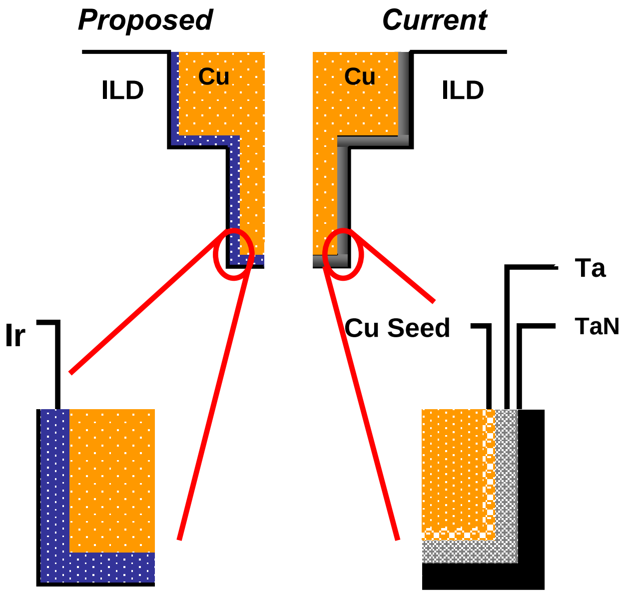

Figure 2-1 Ir as seedless diffusion barrier for Cu interconnects.

Iridium metal is a hard transition metal element with a high meting point of 2466°C, and an unusually high resistance to corrosion. Its face-centered cubic crystalline structure with high electrical conductivity (4.7 μΩ·cm) is thermally stable up to 700°C, meaning that it does not form other compounds up to this temperature when in contact with other elements. Other applications have been found as micro-sensors [10], electrodes for methanol oxidation [11] and ferroelectric non-volatile random access memories. The deposition of copper on iridium has been characterized through electrochemical techniques, x-ray photoelectron spectroscopy, x-ray diffraction, and scanning electron microscopy [9]. It could be concluded that iridium is amenable to direct copper electroplating with no seed layer needed and allows for precise potential control, important for efficient bottom-up copper electrofill of dual-damascene features when processing interconnect devices. Furthermore copper showed a strong adhesion to iridium surfaces when annealed to 600°C, and overall stability. Additionally, this kind of studies where made with iridium barrier layers deposited by atomic layer deposition and scanning electron microscopy, and the results demonstrated that these permit copper wetting and superfill during electrodeposition without the need for a copper seed layer [12]. Therefore the importance of the study of copper under-potential deposition on iridium is evident since it would allow controlled superfilling on sub-micrometer trenches with a stronger binding of the copper to the iridium metal.

In this chapter the copper under-potential deposition on iridium is studied by means of cyclic voltammetry, linear sweep voltammetry, and x-ray photoelectron spectroscopy. The presence of copper under-potential deposition is observed on iridium but not on its thick electrochromic iridium oxide as previously observed on ruthenium oxide; although results show that lower oxidation state iridium oxide (or native oxide) is a good conductor that allows copper deposition. The particular behavior of iridium and iridium oxide towards copper deposition is examined, and the effect of copper concentration, scan rate, and pH is considered. Results account for the limiting nature of copper under-potential deposition process, and increased hydrogen concentration in solution results in copper nucleation at the under-potential region. Interestingly, at pH different than acidic, a particular phenomenon is observed that is associated with the formation of basic copper sulfates or artificial patinas, which has been previously observed when copper is deposited at pH 5 on platinum and ruthenium substrates.

Thermodynamic information shows how copper under-potential deposition is indeed favored on the iridium substrate to a greater extent than substrates like platinum or even ruthenium and its oxides. The strong binding of the copper under-potential deposition to the iridium substrate, and the small amounts at which this occurs, are qualities that make iridium meet the nano scale conditions favorable for the miniaturization of on-chip interconnects.

2.2 Experimental

Ir ESPI[*] shots were made into disks electrodes as previously described in Chapter 1. The shots were polished to mirror finish by different grit silicon carbide (SiC) pads (Allied®[†]), followed by soaking for seven minutes in aqua regia, and electrochemical cleaning in sulfuric acid. A platinum sheet counter electrode, a mercury/mercurous sulfate (Hg/Hg_2SO_4 or MSE) or silver/silver chloride (Ag/AgCl) with a potential shift of 0.660 V and 0.197 V respectively vs. the

---

[*] Electronic Space Products Incorporated, http://www.espi-metals.com
[†] Allied High Tech Products Incorporated, http://www.alliedhightech.com

standard hydrogen electrode (SHE) were employed. All potentials here in referred, including the potentials presented in the cyclic voltammetry curves, are reported versus the Ag/AgCl reference electrode, except for the experiments related to basic copper sulfates formation and iridium oxide growth where MSE reference electrode was employed.

High purity copper sulfate (99.9 %) and potassium sulfate (99.0 % minimum) from Aldrich®[*], 96.2 weight % sulfuric acid and sodium hydroxide (both from Mallinckrodt Baker, Inc. ©[†]) were used to make all electrolyte solutions in ultrapure water (18.2 MΩ, Millipore©[‡]). All solutions were purged with argon for 10 minutes. Electrochemical investigation was performed using a 440 and 400 series model electrochemical analyzer from CH Instruments, Inc. ©[§]. Cu plating on Ir electrodes was carried out under argon atmosphere in order to avoid presence of native oxides on the surface.

Hydrous Ir oxide was prepared electrochemically by potential cycling of a freshly prepared Ir electrode between -0.200 V and 1.300 V vs. Ag/AgCl for 250 complete cycles in aqueous sulfuric acid solution. This is different from how the oxide is formed for Pt or Ru, given that the oxide does not grow at constant potential since an electrical field across the oxide is needed to support ionic transport necessary for growth to occur [31, 32].

---

[*] Sigma Aldrich Corporation, http://www.sigmaaldrich.com
[†] Mallinckrodt Baker, Inc. http://www.mallchem.com
[‡] Millipore Corporation, http://www.millipore.com
[§] CH Instruments, Inc. http://www.chinstruments.com

The potential limits used to obtain the cyclic voltammograms for the iridium electrode from both the background electrolyte and the copper containing solutions, are -0.100 V and 0.450 V where the copper under-potential deposition and the initial growth of copper bulk overlayers (not complete, since it is not the subject of study) are observed.

The open circuit potential for the iridium electrodes is between 0.430 V and 0.520 V vs. Ag/AgCl for both background electrolyte and copper containing solutions; these values were employed as the initial potentials in the cyclic voltammograms. All experiments were performed at a scan rate of 20.0 $m{\cdot}Vs^{-1}$ and room temperature, except for the cyclic voltammograms where the objective is to observe the influence of scan rate on the under-potential deposition of copper. Additionally, the scan rate was varied to 50.0 $m{\cdot}Vs^{-1}$ when growing the thick iridium oxide film.

The geometric area of the iridium electrode is 0.340 cm^2 and the electroactive area corresponds to 0.430 cm^2, which is obtained by means of Randles-Sevcik equation (6) from data obtained from cyclic voltammetry profiles of the iridium electrode in potassium ferro-cyanide solution. With this information the cyclic voltammograms could be plotted as potential versus current density.

XPS data were collected using a VG®[*] ESCALAB MKII spectrometer (VG Scientific Ltd) with an Al Kα x-ray as the excitation source as explained in

---

[*] Thermo Electron Corporation, http://www.thermo.com

Chapter 1. The images were recorded in dark field at different magnifications using a microscope (Nikon® ME600L[*]).

2.3 Copper Under-Potential Deposition on Iridium

2.3.1 Results

Figure 2-2 shows CV scan for clean Ir electrode immersed in a 0.5 M H_2SO_4 solution in the range potential where the Cu UPD and OPD can be easily distinguished.

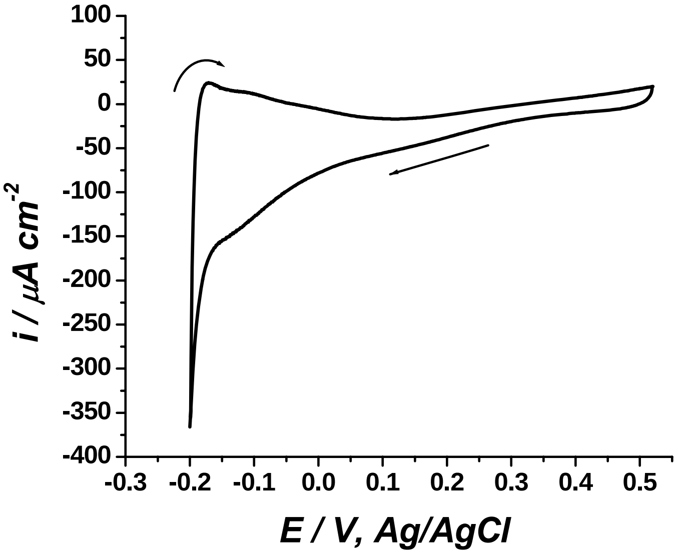

Figure 2-2 CV profile of the Ir electrode immersed in aqueous 0.5 M H_2SO_4 after cleaning procedure.

---

[*] Nikon Corporation, www.nikon.com

The CV scans started at the open circuit potential of the Ir electrode in this solution, 0.520 V vs. Ag/AgCl, and continuous cycling was made in order to obtain reproducible CV scans that would ensure proper electrochemical cleaning of the Ir surface. Additionally, at each cathodic scan the potential was held at -0.100 V to reduce the surface since the presence of native iridium oxides has been observed at 0.450 V [13] that would interfere with the Cu UPD. The final potential of the CV was that of 0.520 V in the anodic scan.

Figure 2-3 show the CV scan for the Ir electrode in 2 mM $CuSO_4$ solution dissolved in 0.5 M H_2SO_4 where both Cu UPD and OPD are observed.

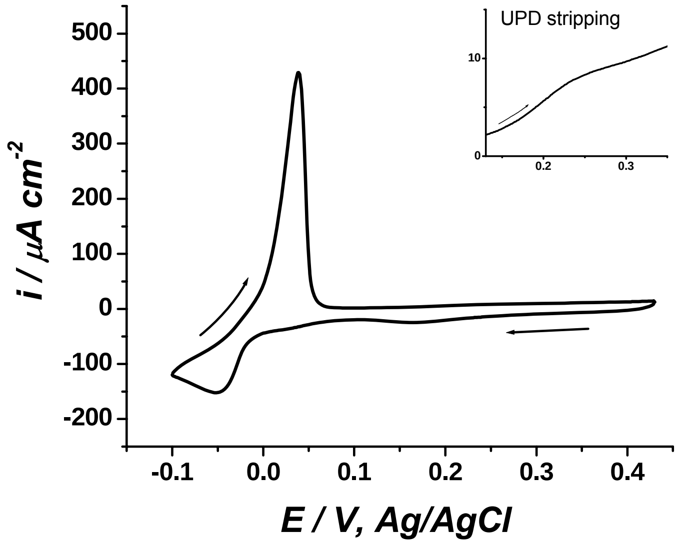

Figure 2-3 CV profile of the Ir electrode immersed in

2 mM $CuSO_4$ / 0.5 M H_2SO_4.

The CV scan starts at OCP of 0.430 V and moved towards negative potentials where the UPD region is found between 0.250 V and 0.0500 V, with a peak potential of E_p = 0.160 V. The Cu OPD overlayers start to deposit at 0 V, and would deposit in larger amounts if the scan is allowed to go to more negative potentials. In the reverse scan the Cu OPD stripping peak has E_p = 0.0400 V, and is completely removed at 0.0700 V. The insert shows the anodic portion of the Cu UPD stripping peak which is not is not a very well defined peak in the anodic scan that has a E_p = 0.240 V. The final potential of the CV was that of 0.430 V in the anodic scan.

Figure 2-4 shows a series of progressive CV scans that allow observing the growth of Cu UPD.

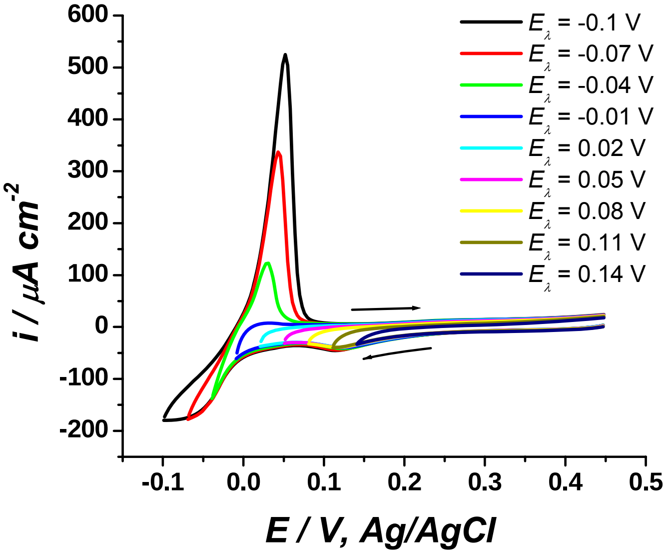

Figure 2-4 Progressive CV profiles of the Ir electrode at different E_λ.

The initial potential was that of the OCP, 0.450 V vs. Ag/AgCl, and moved progressively negative to different *E_λ* every 30.0 mV starting at 0.140 V and going cathodic to -0.100 V. The Cu UPD peak was observed in the potential range of 0.250 V to 0.0500 V, and the peak potential is found at E_p = 0.120 V. Cu OPD is obvious at -0.0400 V, and the Cu OPD stripping is found in the anodic scan at 0.0500 V. With a very light peak the Cu UPD stripping region is observed between 0.370 V to 0.180 V.

Figure 2-5 show the CV scan in the potential region corresponding to Cu UPD in 2 mM $CuSO_4$ / 0.5 M H_2SO_4.

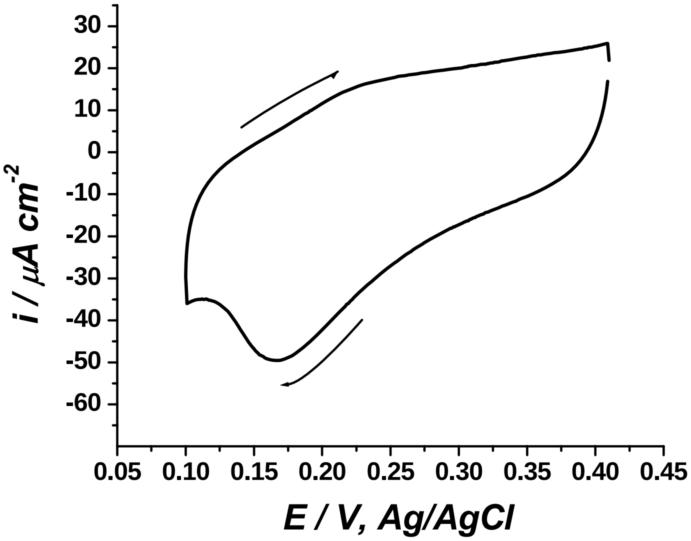

Figure 2-5 CV profile of the Ir electrode in the Cu UPD region.

The cathodic E_p = is found at 0.170 V, and the current associated with this peak corresponds to 9.73 x10^{-5} C·cm^{-2}; it may be possible that this peak found in the potential range of 0.275 V to 0.100 V corresponds to a combination of oxide reduction and Cu UPD which will be discussed in further detail in section 2.3.2.

Additional CV scan was obtained from the Ir electrode in a 2 mM $CuSO_4$ / 0.5 M H_2SO_4 that was previously purged by hydrogen gas for 15 minutes to reduce the presence of oxygen, and to observe the effect on Cu UPD. The results are shown in Figure 2-6.

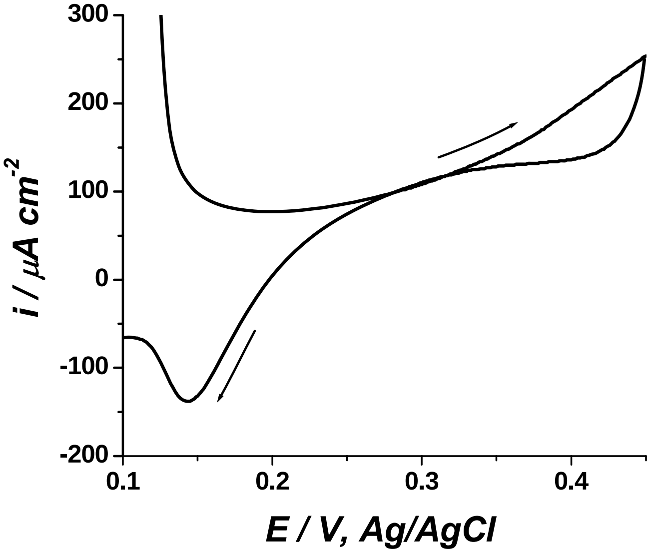

Figure 2-6 CV profile of Cu UPD region from 2 mM $CuSO_4$ / 0.5 M H_2SO_4 after 15 minutes of H_2 purge.

The UPD process has the characteristic of being a limiting one that is kept constant independently of concentration or scan rate [7]. Figure 2-7 shows a series of CV scans performed at different concentrations in order to observe the behavior of Cu UPD, where the initial potential was that of the OCP, 0.430 V. The CV scans were obtained from 2 mM, 5 mM, 10 mM, and 20 mM $CuSO_4$ solutions prepared in the 0.5 M H_2SO_4 electrolyte. The insert in Figure 2-7 shows the potential region corresponding to Cu UPD at the aforementioned concentrations, where the Cu UPD shows a slight variation in peak potential but it is similar in shape and size.

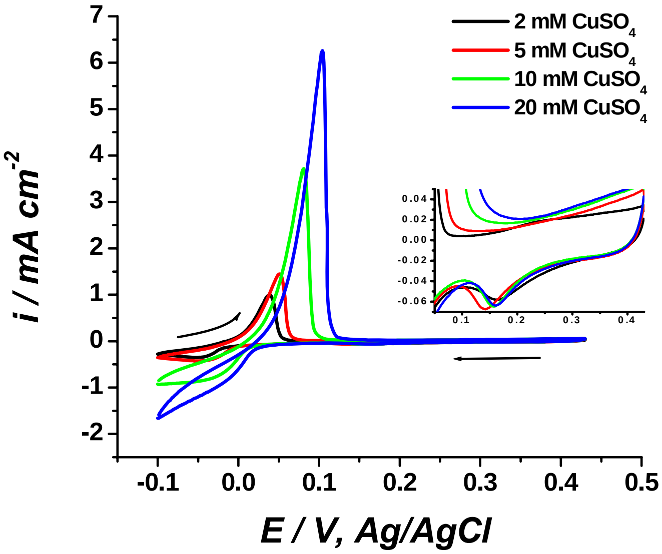

Figure 2-7 CV profiles of the Ir electrode at different concentrations. Insert shows Cu UPD region.

Figure 2-8 shows CV scans at different scan rates in the 2 mM $CuSO_4$ / 0.5 M H_2SO_4 solution or UPD solution. The CV scans were obtained every 20.0 mV·sec^{-1} starting at 20.0 mV·sec^{-1} and moving to higher scan rates up to 140 mV·sec^{-1}; the feature corresponding to Cu UPD is still visible at higher scan rates.

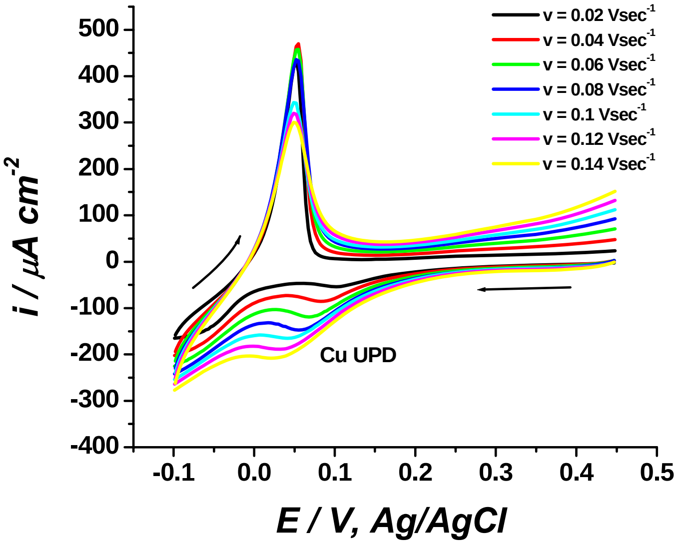

Figure 2-8 CV profiles of the Ir electrode at different scan rates.

In order to confirm the existence of Cu UPD on Ir in the potential region of 0.250 V to 0.0500 V, linear sweep voltammetry (LSV) technique was used in order to obtain a single cathodic scan starting at OCP of 0.450 V, and going to negative potential of 0.0500 V to allow only Cu UPD, and avoiding Cu OPD region. X-ray photoelectron spectroscopy data was obtained from the Cu UPD on Ir, and the results are shown in Figures 2-9 and 2-10.

In Figure 2-9 the energy region for electrons emitted from the Cu 2p orbital is shown in the XPS data [14], and two peaks are observed at 951.9 eV and 932.2 eV.

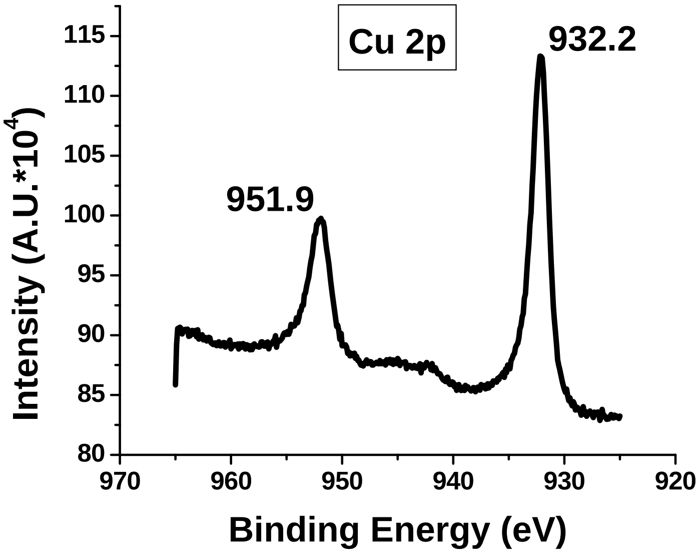

Figure 2-9 Cu 2p region of XPS spectrum corresponding to Cu UPD region.

XPS data is presented in Figure 2-10 that shows two peaks corresponding to the Ir photoelectrons at 64.2 eV and 61.2 eV, and that accounts for the state of the Ir substrate. These results are explained in further detail in section 2.3.2.

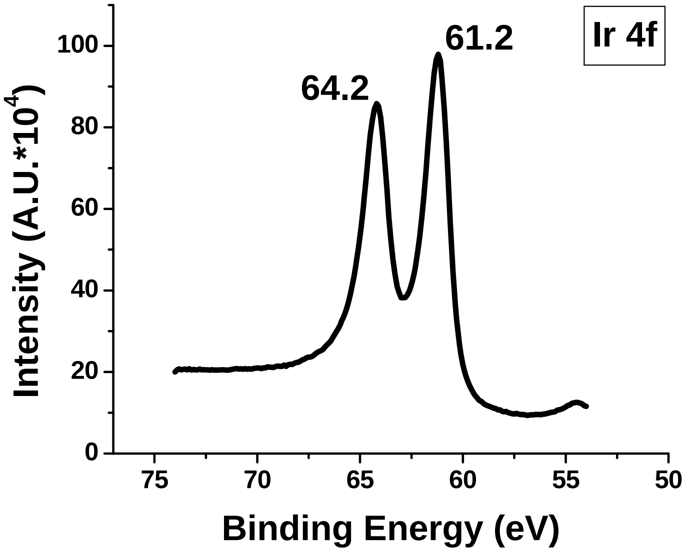

Figure 2-10 Ir 4f region of XPS spectrum corresponding to Ir substrate when Cu UPD is observed.

Additional experiments were made in order to observe the influence of pH in the deposition of Cu. Previous work has proved the existence of basic copper sulfate species like ponsjakite [$Cu_4SO_4(OH)_6 \cdot H_2O$] when the pH is made slightly basic, specially at pH 5.

The existence of these species on Pt and Ru in the anodic potential corresponding to the UPD region has been confirmed by electrochemical quartz crystal microbalance, XPS and x-ray diffraction studies [15, 16], and therefore the pH of the copper containing solution was varied in order to confirm the existence of these species when Ir substrate is used.

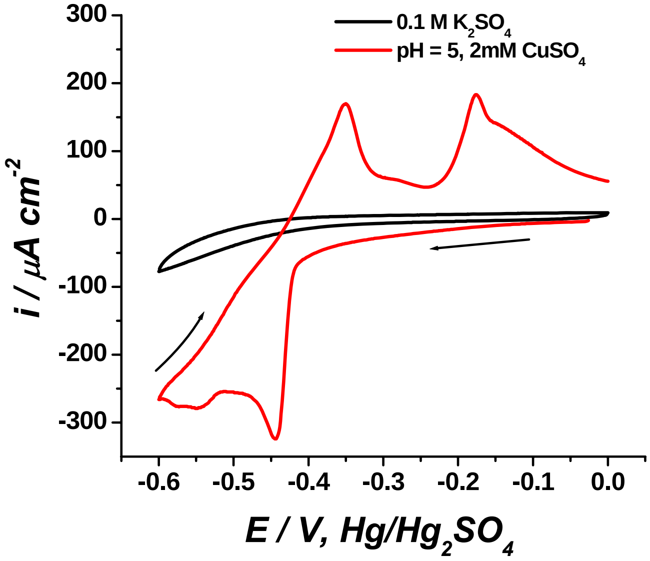

Figure 2-11 Background CV (black) and first CV scan (red) of the Ir electrode in Cu containing solution at pH 5.

Figure 2-11 shows the background CV of Ir in the supporting electrolyte 0.1 M K_2SO_4 together with the first CV in the pH 5 copper containing solution, and Figure 2-12 shows consecutive multiple CV scans that confirm the formation of basic copper sulfates that follows a similar mechanism to the reported one by Zhang and Ojeda [15, 16]. For these experiments the used reference electrode was Hg/Hg_2SO_4 (or MSE), and the initial and final cycling corresponded to OCP, -0.0600 V vs. MSE.

The presence of two well defined peaks labeled C1 and C2 is observed in the cathodic scan that correspond to the anodic features labeled A1 and A2, and that vary with multiple cyclic.

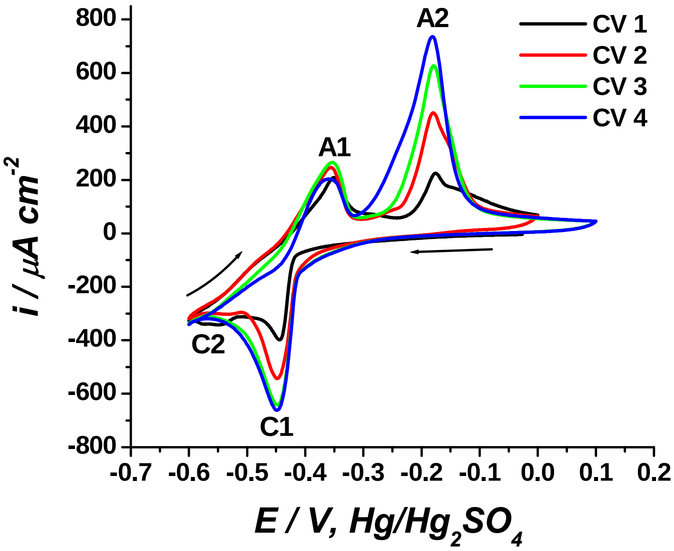

Figure 2-12 Multiple CV scans of Ir electrode from

Cu containing solution at pH 5.

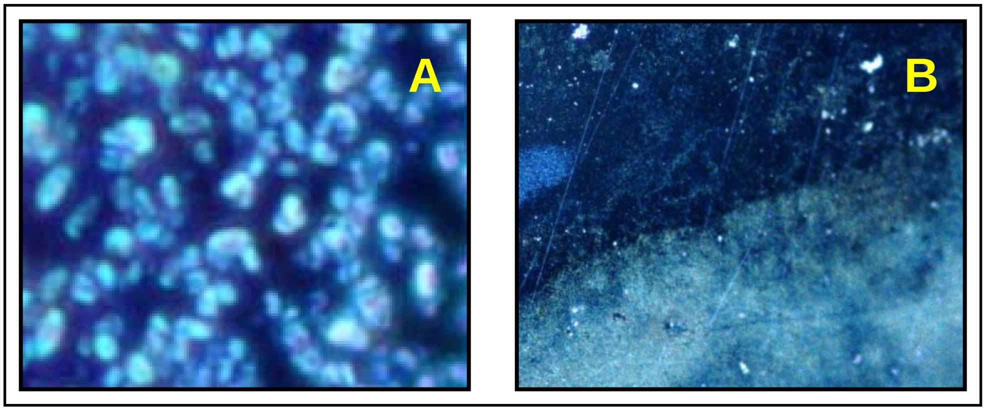

Figure 2-13 Dark field microscope pictures of precipitate formed at A2:

(A) 100X, and (B) 5X magnification.

The precipitation of basic copper sulfates at peak A2 is supported by microscope images presented in Figure 2-13 at different magnifications.

2.3.2 Discussions

Proper polishing and cleaning of the Ir electrode as described in section 2.2 is needed in order to obtain a background CV scan like the one shown in Figure 2-2. Otherwise, improper cleaning would allow oxide residues on the surface that show as a peak at 0.450 V vs. Ag/AgCl (or -0.0100 V vs. MSE), and that can be identified as O_{A1} in Figure 2-14 below, and Figure 2.15 from section 2.4.

The charge associated with the cathodic peak in Figure 2-3 and Figure 2-5 corresponds to approximately 9.73×10^{-5} $C \cdot cm^{-2}$ or 0.304 Cu UPD monolayers assuming that the peak corresponds only to Cu UPD. It is possible that the charge at this peak includes charge contributions from iridium oxide reduction, which as will be explained in detail in section 2.4, can form a native and conductive oxide layer at contact with oxygen saturated environments [18], and which from the cleaning procedure can be significantly reduced.

Figure 2-14 shows the progressive scans for the Ir electrode after exposure to air and from a Cu UPD solution that has not been purged with argon. It is evident the presence of a reversible anodic peak labeled as O_{A1} that may correspond to Ir(OH) species at the surface [18] in amounts that still allow Cu UPD. The Cu UPD is well defined, and it is observed as a broader peak in the anodic scan.

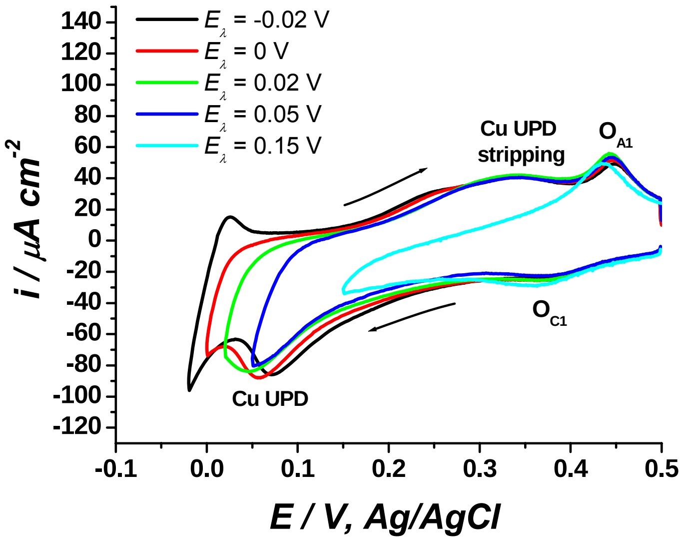

Figure 2-14 Progressive CV profiles of the Ir electrode in 2 mM $CuSO_4$ / 0.5 M H_2SO_4 at different E_λ. The presence of reversible oxide is observed.

From figure 2-14, charge measurements of the anodic peak corresponding to Cu UPD stripping correspond to 1.76 x10^{-4} C·cm^{-2} which corresponds to 0.550 Cu UPD monolayers, and is slightly greater value than the one measured for the pre-cleaned Ir surface. Therefore it can be observed that the polishing procedure together with electrochemical cleaning, do reduce the CV features related with the Ir(OH) species at 0.450 V (Figure 2-5) but does not affect in a great extent the amount of Cu UPD peak. From Figure 2-14 the individual features are observed for Cu UPD and Ir(OH) that account for two different reversible processes; the observed broadness of the Cu UPD stripping as compared to the O_{A1} peak in the anodic scan can explain why the Cu UPD stripping is so minute in Figures 2-3 and 2-5. The Cu UPD is stripped off the surface in the broad potential range of 0.150 V to 0.400 V, appearing to be smaller than the cathodic peak. The somewhat grater Cu UPD amount for the CV in Figure 2-14 suggests a favored Cu UPD on slightly oxidized Ir surface, and from the XPS results that are discussed below it can be conclude that Cu UPD does deposit on the thin native oxide layer of the Ir.

The potential difference between OPD and UPD anodic peaks can be calculated as ΔE_p = 210 mV, and the change in free energy associated with the binding of the Cu UPD monolayer to the Ir substrate can be obtained from:

$$\Delta G = nF\Delta E_p \tag{1}$$

Where F is Faraday's constant (section 1.2), and n is the number of electrons transferred in the reduction-oxidation of Cu:

$$Cu^{2+} + 2e^{-} \rightarrow Cu^{0} \tag{2}$$

Therefore the change in free energy corresponds to $\Delta G° = 40.5\ kJ \cdot mol^{-1}$. This value is larger if compared to published results [7] where the change in free energy associated with the Cu UPD on ruthenium and ruthenium oxide is 21.0 $kJ \cdot mol^{-1}$ and 33.0 $kJ \cdot mol^{-1}$ respectively; the binding of the first monolayer of Cu on Ir would therefore be stronger than on ruthenium and ruthenium oxide.

The progressive CV scans in Figure 2-4 allow observing the Cu UPD growth which occurs completely and free of Cu bulk overlayers if the switching potential is E_λ = 0.0200 V or 0.0500 V. The same kind of CV obtained from H_2 purged solution is shown in Figure 2-6 and the CV scan presents a crossover that occurs between the cathodic and anodic current traces at crossover potential E_X ≈ 0.300 V. This is an indicator that Cu nucleation occurs due to the difference in deposition and dissolution potentials [17] in that region. From [17] it has been shown that Cu bulk nucleation depends on pH and concentration, and further experimentation is needed to confirm if this is true for Cu UPD too; so far it is evident that an increase in H concentration changes the way Cu deposits at under-potential, favoring the nucleation mechanism.

Figure 2-7 shows the CV scans at different Cu^{2+} ion concentrations, which does not cause significant change of Cu UPD coverage on the Ir electrode. These observations are consistent with the surface-limiting nature of UPD process. The peak potentials of Cu bulk did shift 50.0 mV positive as expected when $[Cu^{2+}]$ is increased from 2 mM to 20 mM, and for the Cu UPD just a slight shift was observed. Figure 2-8 shows the effect of scan rate on the Cu UPD, and the observed peaks are clearly visible up to 400 $mV\cdot sec^{-1}$ as expected for UPD process. This is in agreement with the idea that Cu UPD is constant and sometimes favored with higher scan rates, since it is not a diffusion controlled process.

The existence of Cu UPD was confirmed by x-ray photoelectron spectroscopy as shown in Figures 2-8 and 2-9. XPS of the Ir electrode in the copper region is shown in Figure 2-9, where the energy region for electrons emitted from the Cu 2p orbital is shown [14]. This confirms that at 0.0500 V, Cu UPD has occurred. Indeed the value of the peak at 932.32 eV corresponds to Cu $2p_{3/2}$ photoelectrons, and it confirms the existence of metallic Cu.

In Figure 2-10 there are two peaks that account for the state of the iridium electrode after Cu UPD is obtained. The first peak is found at 64.2 eV and it corresponds to Ir $4f_{5/2}$ photoelectrons, and the second one is at 61.2 eV corresponding to Ir $4f_{7/2}$ photoelectrons which interestingly accounts for an oxidized form of the iridium metal with a +1 state. This is an indicator of the existence of the native oxide or hydroxide layer that forms instantaneously on the Ir surface at contact with oxygen even if careful cleaning procedure is made. The cleaning procedure would reduce the CV features related to this native oxide, but this would form as soon as the Ir is in contact with an oxygen saturated environment (either air or solution). This form of conductive Ir(OH) has been well studied in literature, where the formation of a monolayer of this type of oxide is studied when immersing the Ir electrode in a oxygen saturated acidic solution [18], and it has been observed for other noble metals like platinum or gold [33].

Even if the oxide features or O_{A1} features are not present in the CV scans when Cu UPD is observed due to care taken of not to expose the surface to large amounts of oxygen, the XPS data accounts for the very well defined presence of

Ir(OH) species, or what would be the native oxide layer that may have formed at contact of the Ir with the oxygen in solution, or at contact with air after the electrode was taken out from solution and transferred to the XPS chamber for analysis. This proves the strong affinity of Ir to form the native oxide, and the stronger Ir-O bond as compared to Pt-O or Ru-O bond [20] that does not interfere with the Ir-Cu bond, maintaining the metallic nature of the Cu UPD. Since the signals corresponding to metallic Ir are not observed from the XPS data in figure 2-10, it is possible that the Cu UPD occurs on top of a very thin Ir(OH), that is so thin that still does not show the features (O_{A1} peak) in the CV data but from XPS is evident that it is present. Therefore from Figures 2-5 and 2-14 it can be observed that the growth of the Ir(OH) species does not interfere with the amount of Cu UPD to a certain extent.

The precipitation of basic copper sulfates or ponsjakite [$Cu_4SO_4(OH)_6 \cdot H_2O$] [21] is also observed on Ir substrate when the pH of the 2 mM $CuSO_4$ solution is varied and increased to 5 as previously reported on Pt and Ru substrates by Ojeda and Zhang [15, 16]. Figure 2-11 shows the CV scan for the Ir electrode in the 0.1 M K_2SO_4 background electrolyte followed by the first CV scan in the copper containing solution at pH 5. The observed features in the CV scan in Figure 2-11 for Cu deposition differ from those observed in acidic solution in Figure 2-3. The current density associated with the Cu OPD overlayers is significantly smaller in Figure 2-11 if compared to Figure 2-3, and the appearance of a broad peak is observed in the anodic region that corresponds to a reaction different from Cu UPD stripping since the observed current density is very large. In Figure 2-12 these features are observed more clearly after obtaining multiple CV scans of the Ir electrode in the pH 5 copper containing solution. As previously described in references [15, 16], the cathodic peak C1 is associated with a pre-peak to Cu OPD peak C2. Peaks A1 and A2 correspond to Cu OPD stripping and precipitation of basic copper sulfates respectively.

It is interesting to note that multiple scanning in this solution at the same potential limits favor the increase in current density or charge accumulation at the end of each cycle, caused by the appearance of A2; this is not observed at other pH values. This increase in current density at the end of each cycle is related to the precipitation of a blue-white compound that is visible to the eye on top of the Ir electrode, and that is shown to more detail in the microscope images presented in Figure 2-13. XRD has been previously used for characterization of the precipitate [15] and it has shown the pattern characteristic of ponsjakite [22-24] [$Cu_4SO_4(OH)_6 \cdot H_2O$], a form of basic copper sulfate (PDF#43-0670, 83-1410) that it is considered a hydrated form of brochantite [25] which is product of copper corrosion at statues and roofs, better known as patinas. XPS data at different points of the CV scan allowed the identification of metallic Cu, Cu_2O, CuO, and sulfates, assisting in the development of the following mechanism for ponsjakite precipitation:

$$3Cu(OH)_2 + Cu^{2+} + SO_4^{2-} + H_2O \rightarrow Cu_4SO_4(OH)_6 \cdot H_2O \qquad (3)$$

This accumulation of ponsjakite eliminates the presence of active centers in the Pt surface for under-potential deposition of copper, like it has been observed at lower pH values by Danilov [26]. It has been studied by EQCM that on the reverse cathodic scan, a proportional mass desorption or “dumping” appears at potentials close to -0.420 V that corresponds to the dissolution of the basic copper sulfates. The area of the peak C1 increases with the number of cycles, and eventually peak C2 is obscured, meaning that the Cu OPD deposition is also inhibited by the reaction that produces the ponsjakite or artificial patina.

In summary, the following consecutive conditions were met that led to the formation of ponsjakite or artificial patinas: first, cuprite was formed at C1 (-0.400 V) [22] in the cathodic range:

$$2Cu^{2+} + 2e^- + 2OH^- \rightarrow Cu_2O + H_2O \qquad (4)$$

Then, Cu^{2+} ion species were made available through the Cu stripping process present at “A1” potential:

$$Cu^0 \rightarrow Cu^{2+} + 2e^- \qquad (5)$$

Oxygen reduction reaction, occurring on the electrode's surface causing an increase in the available OH^- ions leads to the formation of copper hydroxide $Cu(OH)_2$, on top of the Cu_2O layer [27,28]:

$$Cu^{2+} + 2OH^- \rightarrow Cu(OH)_2 \tag{6}$$

The already mentioned affinity of Ir metal for the adsorption of OH^- ions and the oxygen reduction reaction [20] suggest the Ir substrate is more favorable towards the production of artificial patinas than other substrates.

The precipitate observed at the end of the cycle consisted of ponsjakite formed by the chemical reaction between $Cu(OH)_2$ and Cu^{2+}/SO_4^{2-} shown in equation (3) [29, 15, 16].

2.4 Copper Deposition on Electrochemically Formed Iridium Oxide

2.4.1 Results

Figure 2-15 shows the CV scans that correspond to electrochemically formed iridium oxide. The potential cycling started at OCP value, and continued to observe the features corresponding to iridium oxide formation. For this purpose the reference electrode was changed to Hg/Hg_2SO_4 since it has been reported that the Cl^- ions will stop continuing oxide growth at Ir since it becomes adsorbed at the metal/oxide interface where it obstructs.

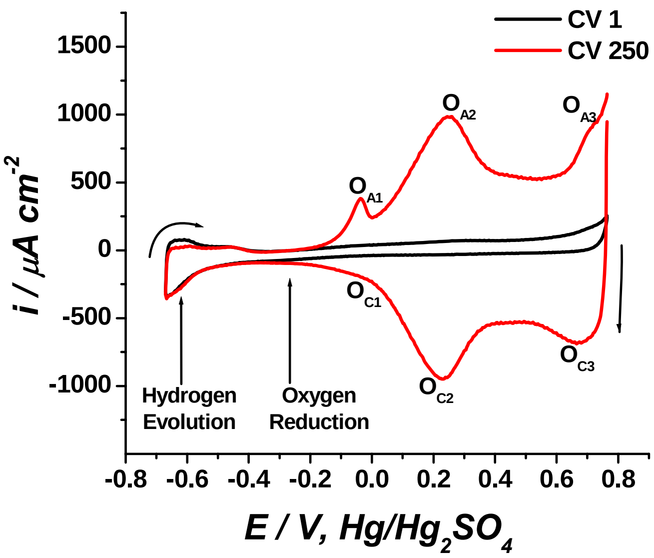

Figure 2-15 Multiple CV scans of Ir electrode in

0.5 M H_2SO_4 to observe iridium oxide growth.

Two main reversible peaks show at -0.0100 V and 0.260 V in the anodic scan, and one more reversible shoulder grows at 0.710 V right before oxygen evolution. The features observed in the growth of iridium oxide have been extensively studied since 1960s and detailed information about this process can be found elsewhere [30, 19, 20].

Figure 2-16 shows the microscope pictures that account for the electrochromic behavior of iridium oxide in acidic solutions. Figure 2-16 (A) accounts for the “bleached state” of the iridium oxide observed at negative potentials or in the cathodic region. Figure 2-16 (B) shows the iridium oxide at positive potentials or in the anodic region which is better known as "colored state".

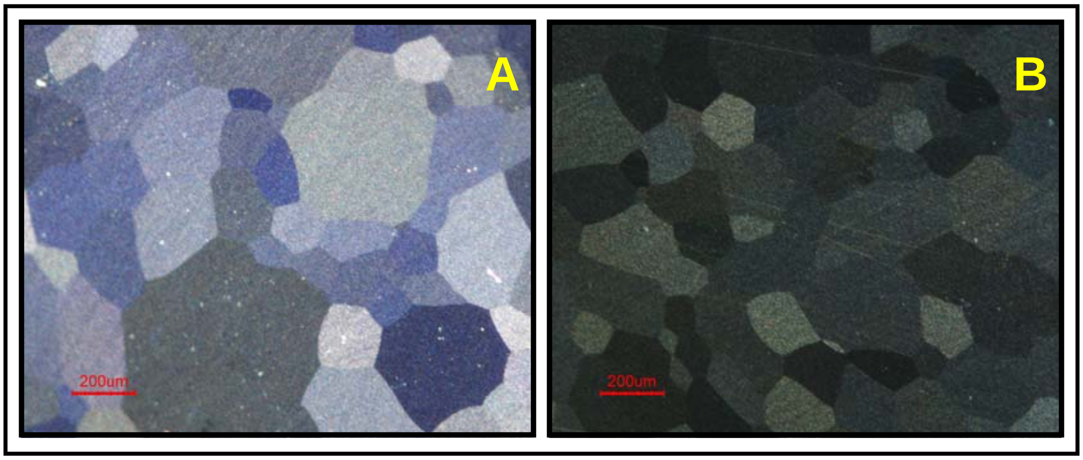

Figure 2-16 Dark field microscope pictures of Ir oxide at 5X magnification: A) Bleached (Insulating), and B) Colored state (Conductive region).

Even though it is known that higher oxidation state iridium oxide is a non conductive oxide in the Cu UPD and OPD regions, additional experiments were made in order to observe its behavior when immersed in Cu UPD solution and confirm this statement.

Figure 2-17 show multiple cycling of electrochemically formed iridium oxide in 2 mM $CuSO_4$ solution that accounts for the limited conductivity of the iridium oxide. These results will be discussed in further detail in section 2.4.2.

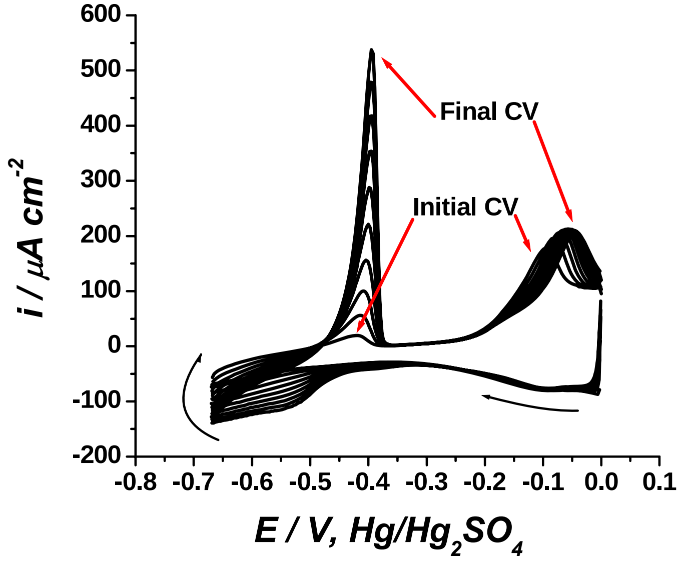

Figure 2-17 Multiple CV scans of electrochemically formed

Ir oxide immersed in 2 mM $CuSO_4$ / 0.5 M H_2SO_4.

2.4.2 Discussions

The features corresponding to Ir oxide formation have been extensively studied and described by different authors [30], especially Conway [19, 20] where three main regions in the anodic potential are identified with the peaks labeled O_{A1}, O_{A2}, and O_{A3} with their corresponding cathodic peaks.

In the cathodic region, the hydrogen evolution region is observed in the potential region of -0.660 V to -0.400 V, and it is identified as H UPD region almost identical to that of the initial metal as observed from the first CV scan and the last scan after multiple cycling. The only difference would account for a decrease in charge by 15-20 % as the oxide grows [19], and this can be observed from the slight decrease in charge observed in that region for the CV scan 250. The double layer charging region is observed between -0.400 V and 0.200 V and it corresponds the one of the Ir electrode, with some overlapping of the oxide reduction reaction.

The peak labeled as O_{A1} is identified as the growth of the first monolayer of iridium oxide or UPD of OH species which has the characteristics of being an almost reversible electrochemical process that involves the development of successive overlay lattices of the thick oxide.

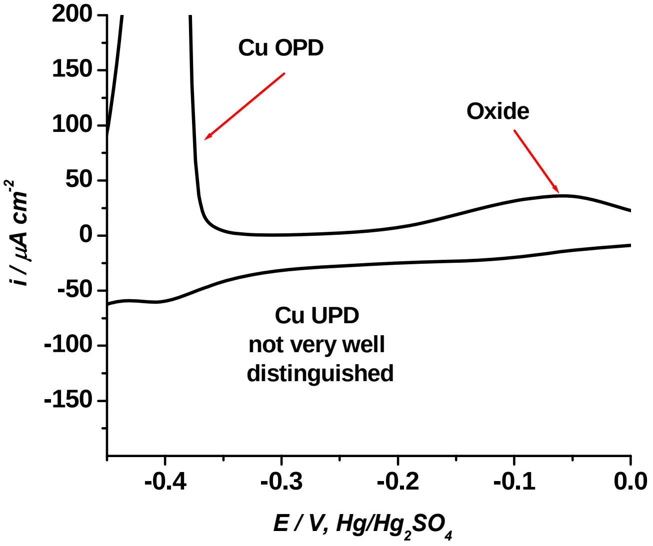

Figure 2-18 Cu deposition when the presence of oxide is observed.

This feature has been observed when trying to deposit Cu UPD if no careful cleaning process has been made as previously described, and a very thin film of this species is always present as a native oxide layer that allows Cu UPD only if thick oxide overlays are not developed. Cu deposition can be observed together with these features as shown in Figure 2-18, confirming that this kind of Ir oxide is conductive and allows good Cu OPD, but limited Cu UPD.

Due to the relatively low potentials at which the iridium oxidation occurs as compared to Ru or Pt, the Ir to oxygen bond is presumably stronger than those corresponding bonds at the mentioned substrates, and the feature associated with the presence of this Ir(OH) monolayer is observed even if the potential has not been high enough to produce a thick oxide [20].

The peak labeled as O_{A2} characterizes the main redox process occurring in the oxide film, corresponding to a $1e^-$ charge associated with the following reaction:

$$Ir(OH)_3 + H_2O \Leftrightarrow Ir(OH)_4 + H^+ + e^- \qquad (7)$$

Or with equivalent unhydrated species Ir_2O_3 and IrO_2. And following O_{A2}, a valley is observed that accounts for the real double layer charge associated with the interface of the porous oxide material. Peak O_{A3} corresponds to further oxidation of the Ir in oxidation state +4 to +5.

These oxides are almost reversible since the growth of the thick film originates from accumulation of incompletely reduced oxide that is left after completion of the cathodic scan, following each cathodic scan. The apparent reversible currents correspond to a redox process within the thick film or on a hyper extended surface, not to the formation of the oxide from the metal or to the reduction of the oxide back to the metal. This behavior is associated with the hysteresis that is observed between the formation and reduction of oxide species when the potential is greater than 0.150 V. Due to the porous, hydrous nature of the thick growing film, the monolayer oxide formation and place exchange process can continue independently on the underlying metal surface.

The microscope pictures in Figure 2-16 show the two states of the iridium oxide when scanned at positive and negative potentials. The oxide can be turned “on” and “off” in the electrochemical sense, since redox process can only take place in this hyper-extended oxide surface at potentials grater than 0.150 V.

Figure 2-16 (A) corresponds to the bleached state of the oxide which is observed at potentials more negative than 0.150 V with the characteristic of being a poor conductor; electrically, the thick oxide film above the metal is turned off in the cathodic region. As shown in Figure 2-16 (B), when the potential becomes more positive, Ir +4 oxidation states are developed in or on the film and the latter becomes a good conductor. Then, all the available double layer capacitance can be charged, the charge for both the inner metal/electrolyte and the oxide/electrolyte interfaces of the pore system.

These changes of state and color (electrochromic effect) in the iridium oxide film are better understood in terms of band structure considerations involving Ir +3 and Ir +4 oxidation states, where the conductivity depends on whether the Fermi level arises in an allowed band (conducting state) or is placed in the middle of a band gap (insulating state).

These features account for the observed results corresponding to Figure 2-17 where it is evident the Cu deposition is not favored on the activated or conductive oxide film due to the different potentials at which each feature is observed. In the multiple CV scans from Figure 2-17 the feature associated with the presence of Ir(OH) and the development thick oxide film is observed in the same potential region, and there is a slight increase in the size of the peak with cycling. This is an indicator that the use of 0.5 M H_sSO_4 background electrolyte makes the oxide grow even if Cu^{2+} species are present in solution.

The gradual increase of the peak associated with Cu deposition is observed at -0.400 V in the anodic scan, and the current density corresponding to this process increases with cycling, meaning that more Cu species are deposited or stripped off the surface with each CV scan.

In the cathodic end of the scan the large amount of electrolyte and Cu^{2+} species available through the pores system at the metal/oxide interface make the metal-electrolyte interface to undergo a charging process that in the absence of Cu^{2+} would be associated with the H and double layer capacitance corresponding to the area of the underlying metal. The applied potential difference falls mainly across the metal/oxide interface, and probably affects the first few layers of oxide close to the metal (O_{A1} peak). For these conditions, Cu is gradually deposited as the Cu^{2+} species permeate through the porous oxide and reaches the possible effective bare metal sites, which have lost 20-30 % of the active sites that have been geometrically blocked by the oxide. Only the Cu^{2+} species being available in the pores of the overlying hydrous oxide film are the ones that interact with the metal for Cu deposition. It is therefore expected to have a constant Cu bulk peak after several multiple scans that would account for the real electroactive area of the Ir metal at those potentials. The large area oxide film that has been developed on the surface or above the metal is turned off under these potential conditions.

Upon further cycling of the oxidized electrode in Cu UPD solution, the Cu OPD peak grows to reach a constant current density, and eventually the film of thick iridium oxide conformed of the mixture of the aforementioned oxides is detached or peeled off the surface.

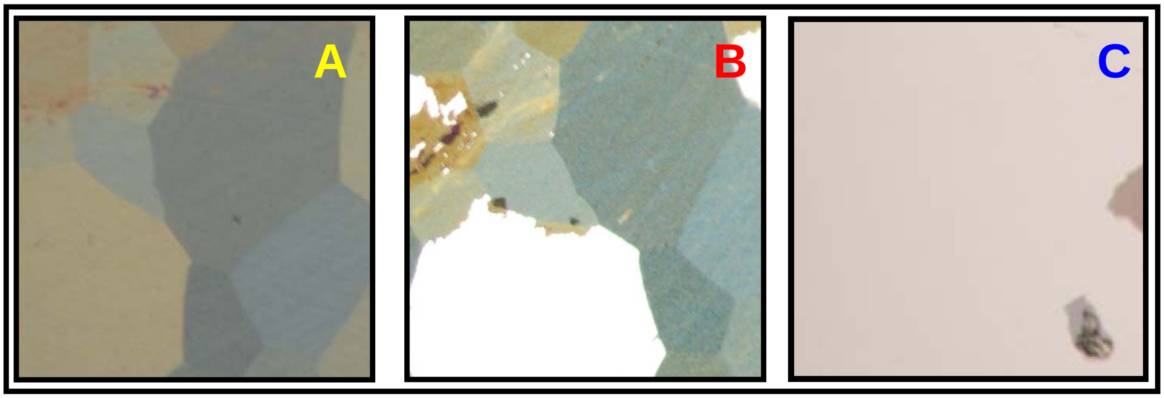

Figure 2-19 Microscope images of thick iridium oxide at 5X bright field: A) before cycling in 2 mM $CuSO_4$; B) after 12 complete cycles in 2 mM $CuSO_4$; C) after further cycling.

This behavior is shown in Figure 2-19 (B), where it is possible to observe the detaching of certain planes of the thick oxide. Further cycling will make most of the thick iridium oxide to be removed from the surface as shown in Figure 2-19 (C).

The amount of Cu OPD observed on iridium oxide reaches a maximum that is very similar in current density to the one observed for Cu OPD on Ir metal or better said on native Ir oxide (compare Figures 2-3 and 2-17). The detaching of the thick oxide does not eliminate some of the features of oxide growth in the CV scan, specifically O_{A1}, since this is observed even when the film is visually off the surface and the Ir metal substrate is clearly observed. This confirms that the peak corresponding to O_{A1} corresponds to the type of native hydroxide layer that in some references mention as very good conductor [18] and the Cu OPD occurs on the native Ir(OH) layer that is thicker than the native Ir(OH) layer that allows Cu UPD.

It is therefore possible to deposit Cu OPD on thicker Ir(OH) film, but it is not the case for Cu UPD, which grows to a limited extent only when the presence of a very thin Ir(OH) film is present. The double layer charging region between -0.400 V and 0.200 V that overlaps with the oxide reduction reaction is approximately the same region that corresponds to Cu UPD; therefore it is possible that the former is dominant over Cu UPD when the thick oxide is grown even if the film has peeled off the surface since the Cu UPD feature is not observed in Figure 2-17.

2.5 Conclusions

In this chapter, the under-potential deposition of copper was studied on iridium substrate by means of cyclic voltammetry, linear sweep voltammetry, and x-ray photoelectron spectroscopy.

The limiting nature of under-potential deposition process was observed for copper on iridium through electrochemical experiments, and results of thermodynamic calculations show a favorable strong binding of the Cu under-potential deposition on the iridium hydroxide substrate. Cu under-potential deposition corresponds to approximately 0.304 to 0.550 Cu monolayers assuming that the cleaning procedure has reduced significantly (but not completely) the presence of the native Ir(OH) species. Further confirmation of results was made by obtaining XPS data.

The influence of hydrogen saturation was observed on the Cu under-potential deposition region where the features of the cyclic voltammetry data correspond to those of a nucleation mechanism for growth. Further experimentation is needed to observe these features in detail. The influence of slightly basic pH in solution was studied, and the growth of ponsjakite was observed on top of the iridium surface; this reaction is favored due to the affinity of iridium metal for OH^- ions and oxygen evolution reaction.

The deposition of copper was studied on iridium oxide, and it is observed that the under-potential deposition is not favored due to the nature of the thick oxide film. Cu over-potential deposition is observed in a particular manner that depends on the porous nature of the iridium oxide film, but does not deposit directly into the thick oxide due to difference in potentials at which Cu deposition occurs and at which the thick iridium oxide film is conductive.

These results are important for the competitive semiconductor industry that is in constant technological development, and search of new materials that can meet the nano scale conditions favorable for the miniaturization of on-chip interconnects. With the presence of a very thin native oxide layer, iridium possesses the characteristics to prevent penetration of Cu interconnect material into the surrounding dielectric; additionally allows electrodeposition of Cu without the use the Cu seed needed due to poor nucleation on some conventionally used barriers.

2.6 References

1. Gerisher, H.; Kolb, D.M.; Przasnyski, M.; *Surface Science* 1974, 43, 662-666.
2. Kolb, D.M., *Advances in Electrochemistry and Electrochemical Engineering,* 1978. John Wiley Interscience: New York. vol. 11. p. 125.
3. Kolb, D.M.; Przasnyski, M.; Gerisher, H.; *Electroanal. Chem. Interfac. Electrochem.* 1974, 54, 25-38.
4. Swathirajan, S.; Bruckenstein, S.; *Electrochim. Acta* 1983, 28(7), 865-877.
5. Van Huong C.N.; Gonzalez-Tejera, M.J.; *J. Electroanal. Chem.* 1988 244, 249-259.
6. Herrero, E.; Buller, L.J.; Abruña, H.D.; *Chem. Rev.* 2001, 101, 1897-1930.

7. Zhang, Y.; Huang, L.; Arunagiri, T. N.; Ojeda, O.; Flores, S.; Chyan, O., *Electrochem. Solid-State Letters*, 2004. 7(9): p. C107-C110.

8. Chyan, O.; Arunagiri, T.N.; Ponnuswamy, T., *J. Electrochem. Soc.* 2003. 150: p. C347.

9. Chan, R., *Interfacial Electrochemistry and Surface Characterization: Hydrogen Terminated Silicon, Electrolessly Deposited Palladium & Platinum on Pyrolyzed Photoresist Films and Electrodeposited Copper on Iridium*. 2003.

10. Jingying, S.; Xuifeng, Xiao; Zeshan, Z.; Xi, Z., *Dianhuaxue*, 1998. 4(2): p. 159-163.

11. Ureta-Zanartu, S.M..; Bravo, P.; Zagal, J.H., *J. Electroanal. Chem.* 1992. 337(1-2): p. 241-51.

12. Josell, D.; Bonevich, J.E.; Moffat, T.P.; Aaltonen, T.; Ritala, M.; Leskelä, M., *Electrochem. Solid-State Letters,* 2006. 9(2): p. C48-C50.

13. Pickup, P.G.; Birss, V.I., *J. Electroanal. Chem.* 1987. 220: p. 83-100.

14. Wagner, C.D., *Handbook of X-Ray Spectroscopy*.

15. Ojeda Mota, O.U., *Interfacial Study of Copper Electrodeposition with the Electrochemical Quartz Crystal Microbalance (EQCM).* 2005.

16. Zhang, Y., Dissertation. 2005.

17. Grujicic, D. and Pesic, B., *Electrochemica Acta*, 2002. 47(18): p. 2901-2912.

18. Hoare, J.P., J. Electroanal. Chem. 1968. 18: p. 251-259.

19. Conway, B.E.; Mozota, J., Electrochim. Acta, 1983. 28(1): p. 9-16.

20. Conway, B.E.; Mozota, J., Electrochim. Acta, 1983. 28(1): p. 1-8.

21. Fitzgerald, K.P.; Nairn, J.; Atrens, A., *Corr. Sci.* 1998. 40(12): p. 2029-2050.

22. Jouen, S.J.,and Hannoyer,B ., *Surface and Interface Analysis*, 2000. 30: p. 145-148.

23. Watanabe, M.; Tomita, M.; Ichino, T., *J. Electrochem. Soc.* 2001. 148(12): p. B522-B-528.

24. Barthelmy, D., *http://webmineral.com/data/Posnjakite.html.* 2004.

25. Helliwell, M. and Smith, J.V., *Acta Crystallographica, Section C.*, 1997. C53: p. 1369-1371.

26. Danilov, A.I.; Polukarov, Yu.M.; Climent, J. M.; Feliu, J. M., *Electrochim. Acta*, 2001. 46: p. 3137-3145.

27. Zerbino, J.O, *Journal of Applied Electrochemistry*, 1997. 27: p. 335-344.

28. Cascalheira, A.C. and Abrantes, M.L., *Electrochimica Acta*, 2004. 49: p. 5023-5028.

29. Christy, A.G., et al., *Journal of Applied Electrochemistry*, 2004. 34: p. 225-233.

30. Rand, D.A.J.; Woods, R., *J. Electroanal. Chem.* 1974. 55: p. 375-381.

31. Stonehart, P.; Angerstein-Kozlowska, H.; Conway, B.E., *Proc. R. Soc. Lond.* 1969. 541: p. A310.

32. Woods, R., *J. Electroanal. Chem.* 1974. 49: p. 217.

33. Sherwood, P.M.A., *Surface Science*. 1980. 101: p. 619-623.

CHAPTER 3

EFFECT OF DIFFERENT ELECTROLYTES ON SILVER UNDER-POTENTIAL DEPOSITION AT PLATINUM EQCM

3.1 Introduction

After electrochemists started using the electrochemical quartz crystal microbalance (EQCM) in solution [1, 2], one of the most important applications for this instrument has been the investigation of electro-deposition of metals [3, 4]. Of special interest has been the study of under-potential deposition processes on transition metal surfaces [5-7], due to the sensitivity of the EQCM to detect and measure trace mass amounts in the nanograms regime that correspond to these processes.

Silver under-potential deposition on platinum is an interesting and challenging redox process that has been extensively studied with different electrochemical techniques, as well as other more complicated surface analysis instrumentation. Since 1971, Tindall and Bruckenstein [8] studied the silver under-potential deposition from sulfuric acid solutions by voltammetry rotating disk electrodes, and they reported the effect of the platinum surface oxidation on the deposition of silver; it was reported that 2 monolayers of silver would only deposit after the platinum surface had been reduced, and that this under-potential deposition was governed by the potential dependence for the reduction of platinum. After this, a series of publications from different authors studying under-potential deposition of silver on polycrystalline platinum electrodes appeared in attempt to describe the process [9, 10], and to obtain accurate charge calculations corresponding to the silver under-potential deposition and the platinum oxide formation, which is somehow complex due to the occurrence of both reactions in the same potential region [11].

Calculation methods based still on charge measurements [12], as well as x-ray photoelectron spectroscopy and angle-resolved x-ray photoelectron spectroscopy studies [13] were made to identify the potential range at which silver could be deposited at under-potential without any influence from the platinum electro-oxidation reaction. Silver under-potential deposition calculations varied from 1 to 2 monolayers for the different authors working with polycrystalline platinum, and as low as 0.77 monolayers were detected on platinum single crystal electrodes [14].

Although if the EQCM is an extremely helpful technique to study silver under-potential deposition on platinum from electrolytes that promote the electro-oxidation of this transition metal, it has not been widely used for that purpose. The EQCM allows monitoring the silver under-potential deposition and striping from frequency measurements, and could be useful in differentiating from the platinum oxide stripping and formation, even if these two reactions overlap in the same potential region.

Iwata and Sasaki have studied silver deposition by means of the EQCM in combination with Atomic Force Microscopy, and results regarding under-potential deposition were not reported [15]. Jeffrey and Harrington have provided with a more detailed report where they use the EQCM to study silver and copper under-potential deposition from perchloric acid solutions [16]; they provide with a detailed analysis of mass-responses for copper and silver deposition with and without iodine, and propose the silver under-potential deposition on iodine covered platinum electrodes as an ideal calibration system for the EQCM.

The effect of different anions in solution on the under-potential deposition of silver and the platinum oxide formation is a topic that has not been extensively studied by means of the EQCM. Uchida and Watanabe have studied the halide adsorption from salts on gold single crystal EQCM [17], and Bruckenstein and Jusys have also used this technique to study adsorption of perchlorate and perrhenate ions on polycrystalline gold [18]. For platinum, only Santos and Machado [19] have studied the anion adsorption on polycrystalline platinum by EQCM from perchloric, sulfuric, phosphoric, and hydrochloric acids; they identified the ions deposited on the surface and calculated the amount of each, but they did not analyze the effect of the electrolytes on the amount of platinum oxide produced since it is not the purpose of the publication.

In this chapter, the under-potential deposition of silver on platinum EQCM is studied due to the complexity of this system especially in the platinum oxide formation region. The effect of different anions present in solution are studied in order to observe their influence in the potential region corresponding to silver under-potential deposition and platinum oxide formation and on the amount of silver deposited at underpotential. This study includes experimentation with perchloric, sulfuric, and phosphoric acid since these electrolytes favor the electro-oxidation of platinum [19]. The platinum electro-oxidation has been additionally explored in hydrochloric acid, but this electrolyte would not be used for this study due to the favored precipitation of silver chloride into solution, which interferes with the oscillation of the quartz crystal. Experimental results in this work indicate that silver under-potential deposition is close the one monolayer in the three different electrolytes, and when phosphoric acid is used, the growth of silver (II) oxide is observed due to the growth and reaction of low coverage hydrous oxide species at potentials prior to the start of the monolayer oxide region, which can be of interest to the fabrication of micro-sensing devices for the detection of contaminants, and to the production of silver oxide for its use as bactericidal.

3.2 Experimental

Electrochemical investigation was performed using a 440 and 400 series model electrochemical analyzer from CH Instruments, Inc. ©[*]. With their corresponding reference oscillators (CH Instruments, Inc.©[*]) vibrating at 7.99 MHz, the time resolved instrument can simultaneously read the frequency

---

[*] CH Instruments, Inc. http://www.chinstruments.com

change of the quartz crystal along with the electrochemical current change on the electrode surface.

AT-cut quartz crystals with a fundamental frequency oscillation of 7.99 MHz where purchased from International Crystal Manufacturing ©[*], with 1.00 x10^3 Å thick polycrystalline platinum electrodes deposited on a 100 Å thick titanium adhesion layer. The oscillating frequency of the crystal is subtracted from that of the aforementioned reference oscillator during EQCM operation.

The crystal itself, bonded to a metallic mount is seated on the bottom of a Teflon®[†] cell, with its surface facing the body of the solution as previously shown in Figure 1-13. The abovementioned platinum EQCM was used as the working electrode in a conventional three way electrode cell. A platinum coil counter electrode and a saturated mercury/mercurous sulfate (Hg/Hg_2SO_4 or MSE) with a potential switch of 0.647 V vs. the standard hydrogen electrode (SHE) were employed. All potentials here in referred, including the potentials presented in the cyclic voltammetry curves, are reported versus the MSE reference electrode.

By means of the Sauerbrey's equation [37], the change in frequency is related to the change in mass:

$$\Delta f = C_f \Delta m \tag{1}$$

---

[*] International Crystal Manufacturing Co., Inc. http://www.icmfg.com

[†] Du Pont, http://www.teflon.com

The sensitivity factor C_f is determined by various properties of the crystal [29, 30] like its thickness, fundamental frequency, and density as mentioned in section 1.3.3. In the case where crystals have a fundamental frequency oscillation of 7.99 MHz the value of the sensitivity factor is 1.42 x10^{-9} Hz·ng^{-1}.

96.2 weight % sulfuric acid, 69.7 weight % perchloric acid, and 85.0 weight % phosphoric acids (Mallinckrodt Baker, Inc. ©[*]) were used to make all background electrolyte solutions in ultrapure water (18.2 MΩ, Millipore©[†]). High purity silver nitrate (99.9 % pure) from Mallinckrodt Baker, Inc. ©[*] was used to prepare the solutions corresponding to the silver under-potential deposition studies. All solutions were purged with nitrogen gas for 10 minutes.

The potential limits used to obtain the cyclic voltammograms for the platinum EQCM from both the background electrolytes and the silver containing solutions, are -0.640 V and 0.80 V, where the complete hydrogen evolution reaction is observed together with the anion adsorption and desorption reactions [19], and the platinum electro-oxidation and reduction [20] together with the silver under-potential deposition[11]. The abovementioned features are observed at approximately the same potentials independently of the electrolyte employed.

The open circuit potential for the platinum EQCM electrodes is approximately the same value when immersed in the three different electrolytes: 0.280 V, 0.290 V and 0.260 V for 0.5 M sulfuric, 0.5 M perchloric and 0.5 M phosphoric acids respectively, and these values were employed as the initial

---

[*] Mallinckrodt Baker, Inc. http://www.mallchem.com
[†] Millipore Corporation, http://www.millipore.com

potentials in the cyclic voltammograms. In the case of the silver containing solutions, the open circuit potentials in the three different electrolytes where 0.310 V, 0.280 V, and 0.280 V for sulfuric, perchloric and phosphoric respectively, and these values were also employed as the initial potentials for the cyclic voltammograms. All experiments were performed at a scan rate of 50.0 $mV \cdot s^{-1}$ and 20.0 $mV \cdot s^{-1}$, and at room temperature.

The geometric electrode area for the platinum EQCM is 0.265 cm^2 from where 0.205 cm^2 correspond to the area of the disk, and 0.06 cm^2 are from the flag of the electrode. The electroactive area corresponds to 0.35 cm^2 for the platinum EQCM data in sulfuric acid, 0.33 cm^2 in perchloric acid, and 0.31 cm^2 in phosphoric acid. These areas were calculated from the under-potential hydrogen charge density corresponding to each electrolyte, together with the surface roughness factor that is equivalent to 1.32075, 1.24528, and 1.16981 for sulfuric, perchloric and phosphoric acids respectively [28]. It is important to note that the electroactive area corresponding to the circular pad where the mass sensing area is encountered corresponds to 0.270 cm^2, 0.255 cm^2 and 0.240 cm^2.

3.3 Effect of H_2SO_4, $HClO_4$ and H_3PO_4 Electrolytes on the Electro-oxidation of Pt EQCM

3.3.1 Results

Figure 3-1 (A) shows cyclic voltammetry (CV) scan for a clean Pt EQCM immersed in a 0.5 M H_2SO_4 solution. The CV scans started at the open circuit potential of the Pt EQCM in this solution, 0.280 V vs. MSE, and continuous cycling was made in order to obtain reproducible CV scans that would ensure proper electrochemical cleaning of the platinum surface. The final potential of the scans was that of -0.400 V in the anodic scan, right after the completion of the hydrogen evolution reaction in order to avoid the presence of oxide or anions for the silver experiments.

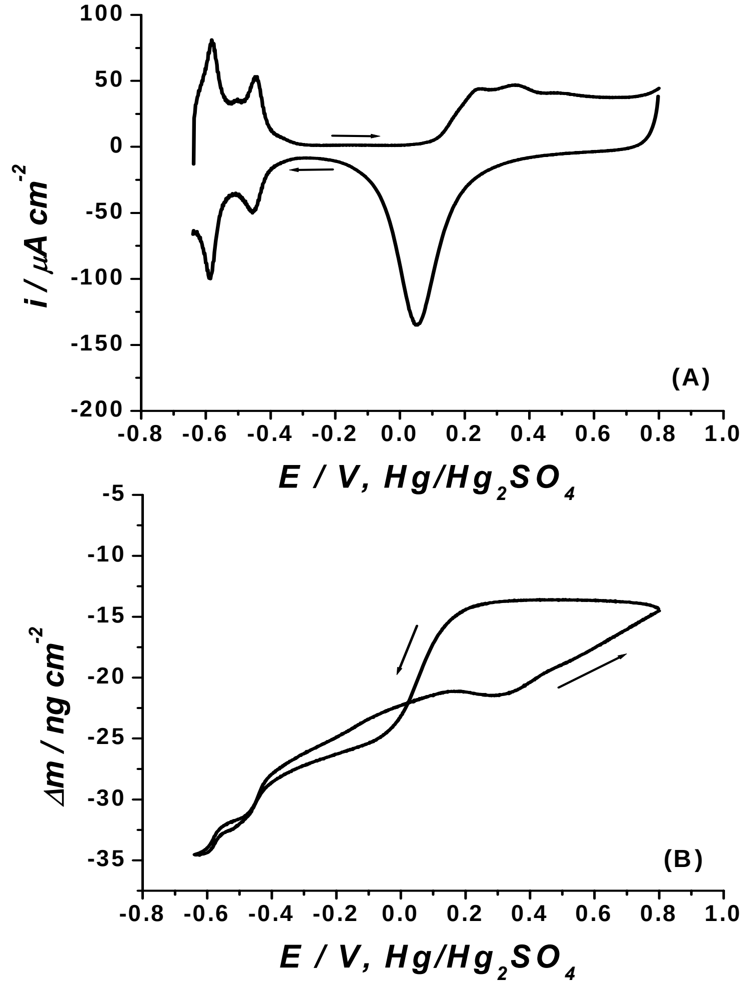

Figure 3-1 CV profile (A) and mass-response (B) for a Pt EQCM electrode in 0.5 M aqueous H_2SO_4.

In the anodic scan the double layer region is visually identified in the potential range of -0.400 V to 0.200 V, and it is associated with the adsorption of $HSO_4^- \cdot 2H_2O$ according to calculation made by Santos et al [19]. The onset of platinum electro-oxidation appears to be at 0.200 V and continues to the anodic switch potential of 0.800 V. In the cathodic scan, the potential region of 0.200 V to -0.100 V associated with the platinum oxide electro-reduction region is observed, where the peak potential for the platinum electro-reduction region reaches a maximum peak current at 0.054 V. A switch potential of -0.640 V is reached in the cathodic scan in order to allow monitoring the complete hydrogen evolution reaction from where the electroactive area of the Pt EQCM was obtained.

Figure 3-1 (B) shows the corresponding mass-response for the CV scans in Figure 3-1 (A), where it is possible to confirm the aforementioned regions by identifying the corresponding mass changes. In the anodic scan, a light mass increase between -0.420 V to 0.200 V is related to the double layer region. This is followed by a more defined mass increase at 0.300 V that is associated with the onset of platinum electro-oxidation (observed as 0.200 V from CV scans), which continues to the switch potential of 0.800 V. In the reverse scan, the onset of oxide reduction is observed at 0.200 V as a decrease in the mass that prolongs with a steep slope to -0.100 V; half way of this region, the potential corresponds to 0.0500 V which accounts for the peak potential of the platinum electro-reduction observed in the CV scans. A continuous and less pronounced mass decrease is observed from this potential down to -0.400 V that is related to the desorption of the $HSO_4^- \cdot 2H_2O$ anions.

Figure 3-2 (A) shows the CV scans obtained when immersing the Pt EQCM into 0.5 M $HClO_4$ solution, where the measured open circuit potential was 0.290 V.

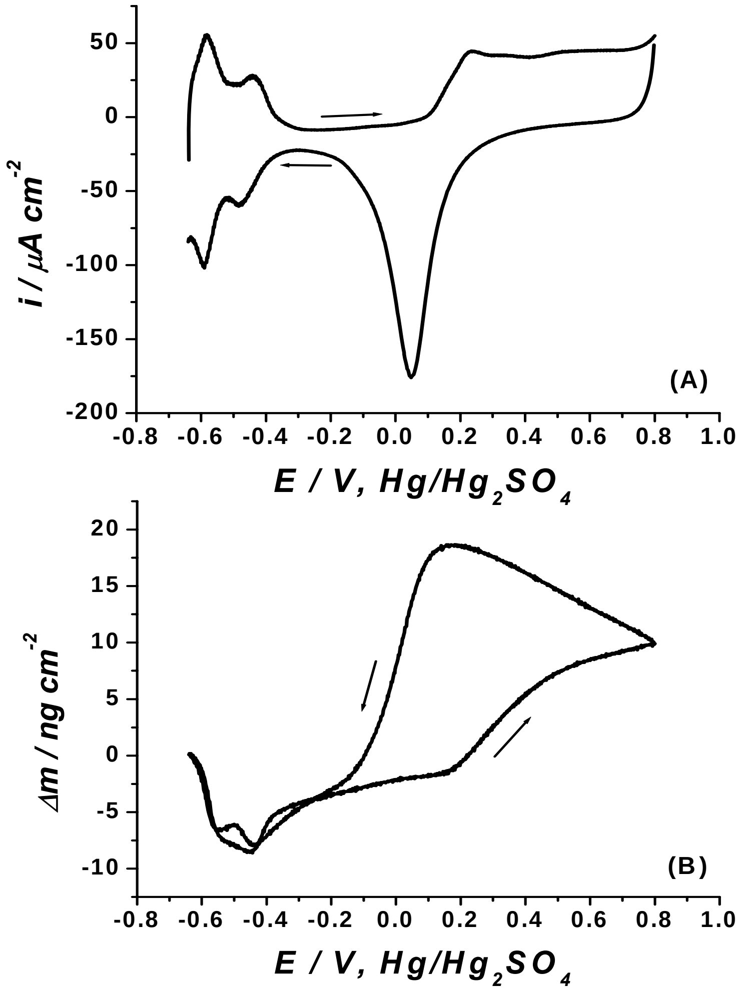

Figure 3-2 CV profile (A) and mass-response (B) for a Pt EQCM electrode in 0.5 M aqueous $HClO_4$.

The CV scans started at the previously mentioned OCP value, and continuous cycling was made in order to obtain reproducible CV scans that correspond to a clean platinum surface. For the present case, the final potential of the scans was that of -0.430 V in the anodic scan, right after the completion of the hydrogen evolution reaction.

The same features that were observed for Pt EQCM in 0.5 M H_2SO_4 are present for the case of 0.5 M $HClO_4$, occurring at slightly different potentials. In the anodic scan the double layer region is visually identified in the potential range of -0.400 V to 0.150 V and it is associated with the adsorption of $ClO_4^- \cdot 2H_2O$ [19], which should be weaker than the adsorption of $HSO_4^- \cdot 2H_2O$ as indicated by the earlier onset of platinum oxidation at 0.150 V. The platinum electro-oxidation continues to the anodic switch potential of 0.800 V. In the cathodic scan, the potential region of 0.200 V to -0.200 V associated with the platinum oxide electro-reduction region is observed, where the peak potential for the platinum electro-reduction region reaches a maximum peak current at 0.048 V. A switch potential of -0.640 V is reached in the cathodic scan as mentioned for H_2SO_4.

Figure 3-2 (B) shows the corresponding mass-response for the CV scans in Figure 3-2 (A). In the anodic scan, a light mass increase between -0.430 V to 0.150 V is related to the double layer region. This is followed by a more defined mass increase that starts at 0.150 V, associated with the onset of platinum electro-oxidation, which continues to the switch potential of 0.80 V. In the reverse scan, the onset of oxide reduction is observed at 0.170 V as a decrease in the mass that prolongs with a steep slope to -0.120 V; half way of this region, the potential corresponds to 0.0250 V which accounts for the peak potential of the platinum electro-reduction observed in the CV scans (observed as 0.0480 V). A continuous and less pronounced mass decrease is observed from this potential down to -0.400 V that is related to the desorption of the $ClO_4^- \cdot 2H_2O$ anions.

The CV scan obtained for the Pt EQCM in 0.5 M H_3PO_4 is shown in Figure 3-3 (A), where repetitive cycles where made starting at the open circuit potential of 0.260 V. In this case the final potential was 0.440 V, at the completion of the hydrogen evolution region.

For Pt EQCM in 0.5 M H_3PO_4, in the anodic scan the double layer region is visually identified in the potential range of -0.400 V to 0.200 V, and it is associated with the adsorption of HPO_4^{2-} [19]; observing the insert in Figure 3-3 (A) it is possible to detect a very small protuberance at -0.150 V, which has been reported as premonolayer oxidation that occurs for platinum immersed in this electrolyte [23]. The onset of platinum electro-oxidation is found at 0.200 V and continues to the anodic switch potential of 0.800 V. In the cathodic scan, the potential region of 0.200 V to -0.150 V associated with the platinum electro-reduction region is observed, where the peak potential for the platinum electro-reduction region reaches a maximum peak current at 0.0270 V. A switch potential of -0.640 V is reached in the cathodic scan as previously done.

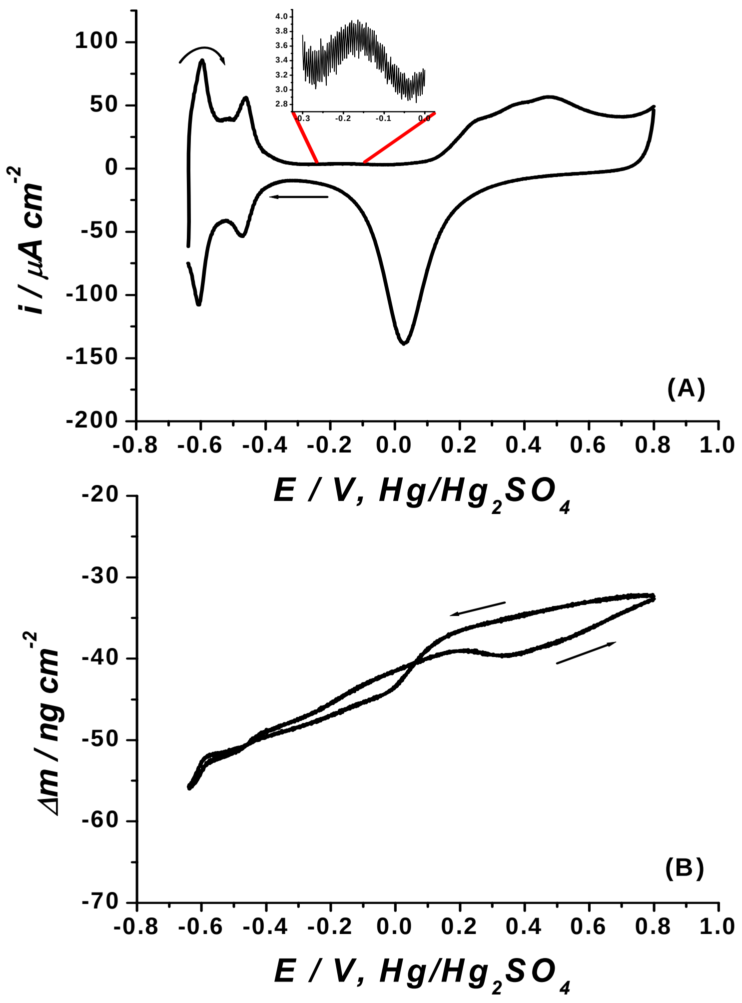

Figure 3-3 CV profile (A) and mass-response (B) for a Pt EQCM electrode in 0.5 M aqueous H_3PO_4.

Figure 3-3 (B) shows the corresponding mass-response for the CV scans in Figure 3-3 (A), where the light mass increase between -0.440 V to 0.300 V (observed as -0.400 V to 0.200 V from CV) is related to the double layer region. This is followed by a more defined mass increase that starts at 0.340 V, associated with the onset of platinum electro-oxidation, which continues to the switch potential of 0.800 V. In the reverse scan, the onset of oxide reduction is observed at 0.150 V, as a decrease in the mass that prolongs to 0 V; in this region, the potential corresponding to 0.0300 V accounts for the peak potential of the platinum electro-reduction observed in the CV scans (observed as 0.0270 V). A continuous and less pronounced mass decrease is observed from this potential down to -0.440 V that is related to HPO_4^{2-} anions' desorption.

3.3.2 Discussions

The features for the CV scans shown in Figures 3-2 (A), 3-3 (A), and 3-4 (A) are in close agreement with results published by Jerkiewicz and Soriaga, where they reexamine the mechanism of oxide growth at platinum electrodes combining cyclic voltammetry and EQCM [20].

Supported with Auger electron spectroscopy data, the following mechanism was proposed by these authors for the platinum electro-oxidation where they exclude the idea that the mechanism involves OH_{ads} as an intermediate. Instead strong water physisorption occurs for a later discharge of $2H^+$ and $2e^-$ that is followed by formation of PtO by an additional reaction with H_2O molecules:

$$Pt + H_2SO_4 \xrightarrow{physisorption} Pt^{\delta+}O^{\delta-}H_2 \tag{2}$$

$$(Pt - Pt) - H_2O \xrightarrow{discharge} (Pt - Pt)^{\delta+}O_{chemisorbed}{}^{\delta-} + 2H^+ + 2e^- \tag{3}$$

$$Pt - O_{chemisorbed} + H_2O \xrightarrow{discharge,exchange,charge\_transfer\_completion}$$

$$(Pt^{2+} - O^{2-})_{quasi-3\_Dlattice} + 2H^+ + 2e^- \qquad (4)$$

This kind of mechanism is one of the two general paths proposed for the surface oxide growth of noble metals by Jerkiewicz in 1999 [25]. In order to identify the species that are adsorbed on the surface of the Pt EQCM, the approximate molecular weights of the species deposited on the double layer and platinum electro-oxidation regions were calculated using the equation proposed in reference [20]:

$$M = \frac{\delta \Delta mnF}{\Delta q} \qquad (5)$$

Where $\delta \Delta m$ is the interfacial mass change between two potential limits,

$$\delta \Delta m = \Delta m_2 - \Delta m_1 \qquad (6)$$

Determined from the EQCM measurements; Δq is the charge density associated with the platinum surface oxidation, n is the number of electrons exchanged in the process, and F the Faraday's constant (9.65 x10^4 C).

The growth of PtO is influenced by the co-adsorbed anions, which to some extent affect the interfacial mass change in the double-layer region. Using a rearrangement of equation (5) that provides with a linear relationship of Δm vs. Δq with a single slope equal to $\frac{M}{nF}$, Santos et al concluded that the mass increase in this region has been associated with the adsorption of $HSO_4^- \cdot 2H_2O$ for sulfuric acid solution, and $ClO_4^- \cdot 2H_2O$ for perchloric acid; in the case of phosphoric acid the species deposited in the double-layer region correspond to HPO_4^{2-} [19]. Equation (5) had previously been used by Uchida et al [36] to analyze anion adsorption on gold from H_2SO_4 and $HClO_4$ electrolyte; therefore it is a commonly used equation for identification of adsorbed species.

Wieckowski and co-workers have showed that these anions desorb at the onset of the surface-oxide growth [21, 27], which is accounted by the different potentials at which platinum oxide starts forming in either sulfuric, perchloric or phosphoric acid. Their results indicate that the anion adsorption on the polycrystalline electrode is a result of adsorption at single crystal micro and macro facets of the polycrystalline surface. These results have also been observed by Campbell and Corn, through more sophisticated techniques like Second Harmonic Generation [31], and You et al. concluded that the process is surface specific and that is different for each crystal platinum surface orientation [22].

Equation (5) can be used directly to calculate the molar mass (M) of the species deposited in the electro-oxidation region. Using the data corresponding to the platinum electro-oxidation region in the CV scan from Figure 3-1 (A), the molecular weight for the deposited species on the Pt EQCM corresponds approximately to that of the addition of one monolayer of oxygen to the interface, 16.2 g·mol^{-1}. This is an indicator that the type of oxide formed is composed of Pt and O in the 2+ and 2- oxidation states respectively. The result is in close agreement with the theoretical value of a monolayer of oxygen deposited on top of the surface. In the case of the perchloric acid electrolyte the calculated value of M is 16.3 g·mol^{-1}, which would also correspond to the oxygen species that start to deposit on the surface at a potential of 0.150 V.

Once it is known that for sulfuric and perchloric acids the kind of platinum oxide species corresponds to PtO, it is possible to measure the mass changes in the platinum electro-oxidation region that are associated with this reaction, and therefore calculate the exact amount of monolayers of PtO that have been formed on the Pt EQCM.

From the mass-response corresponding to Figure 3-1 (B) a change in mass or an increase in mass is observed for the platinum electro-oxidation that corresponds to 8.00 ng of PtO produced in the Pt EQCM. Therefore this amount is associated to approximately 1.14 monolayers of PtO, since it is possible to know that a monolayer of deposited oxygen corresponds to 7.0 ng by the following relationship: the electroactive are that comprises the mass sensing area corresponds to 0.270 cm^2, and per each cm^2 there are 1 x10^{15} atoms, meaning that there are 2.70 x10^{14} atoms in the mentioned area. Then, if there are 6.02

$x10^{23}$ atoms per mol, then there are 4.48 $x10^{-10}$ mol in total that according to the molar mass of oxygen, correspond to 7.00 ng per monolayer of oxygen.

In the case of $HClO_4$, the mass change associated with the platinum oxidation reaction observed from Figure 3-2 (B) is larger than for sulfuric acid since this starts at a more positive potential and continues forming in the cathodic region up to the onset of reduction. The mass increase up to the switch potential is 12.0 ng that corresponds in this case to approximately 1.70 monolayers of PtO taking into account only the mass sensing area of the Pt EQCM corresponding to 0.255 cm^2 in this solution. This is in agreement with the accepted idea that the platinum surface oxidation resulting in PtO species, grows to a limiting thickness of 2 monolayers [26]. Further oxide growth would have developed PtO_2 species with an unknown degree of hydration. Therefore, based on mass-responses and comparing the calculated amounts of PtO formed in perchloric acid solution and sulfuric acid solutions, it is evident that the growth of PtO is favored by perchloric acid solution.

The platinum electro-oxidation in $HClO_4$ solution is somehow different to what has been discussed for sulfuric and perchloric acids. This system has been previously studied by Burke and Morrissey [23], and even if this system is rather similar to the reported for platinum in sulfuric acid, they have noted that platinum oxide could be produced under quite severe conditions like high concentrations (95% H_2PO_4) and high temperatures (160°C), which are relevant to the operation of the oxygen cathode of phosphoric acid fuel cells [24].

In the case of phosphoric acid, the molar mass of the oxygen species that start to form at 0.340 V in Figure 3-3 (A) cannot be calculated as previously done with sulfuric acid and perchloric acid by means of equation (5). It is possible to obtain from the mass-response that the amount of deposited species correspond to 7.00 ng in an electroactive area of 0.240 cm^2, but there are some differences in the way the oxide grows when compared with the aforementioned electrolytes that does not allow to obtain the amount of PtO monolayers as previously done. It is possible that species different than PtO, or a mixture of PtO and other kind of oxides grow on the surface. In reference [23] it is mentioned that the platinum oxide species formed in aqueous phosphoric acid solutions are similar to those reported for gold [34, 35], in the sense that active surface metal atoms oxidize to form low coverage hydrous oxide species at potentials prior to the start of the monolayer oxide (or OH_{ads} and O_{ads}) region; this is the reason why when using formula (5) to obtain the formula weight of the electrodeposited species, the result is something different than the expected 15.9 g·mol^{-1} for oxygen adsorption.

From reference [23] the feature associated with these premonolayer oxidation observations, corresponds to a quite small peak present in the double layer region which can be also be observed in the anodic scan at -0.170 V from the insert in Figure 3-3 (A) when magnifying that region. This feature cannot be distinguished in the cyclic voltammetry profiles obtained from sulfuric and perchloric acid solutions, and therefore accounts for a light difference in the way oxide is produced.

This assumption for premonolayer oxidation in gold has been supported by Desilvestro and Weaver [32], with their surface enhanced Raman spectroscopy studies, where the OH species produced in the premonolayer reaction gave rise to signals that differed from those at the onset of monolayer oxide formation; it is clear from their observations that two hydroxyl species must be involved.

Premonolayer oxidation of platinum can be seen from work reported by Vielstich and coworkers [33], but it will be discussed in more detail in section 3.4 from this study. In general the main problems faced in this area are: 1) the premonolayer oxidation seems to be influenced largely by the defect structure of the surface which is not easily controlled, and where the major factor seems to be the history of the electrode; and 2) the extent of this reaction is usually quite small, and the techniques currently available for the detection of submonolayer coverage OH species are rather limited. Usually the features attributed to this phenomenon may be mistaken as presence of impurities.

Table 3-1 summarizes the observations for the cyclic voltammetry profiles obtained for Pt EQCM in the three different electrolytes.

Table 3-1 PtO Growth in H_2SO_4, $HClO_4$, and H_3PO_4 Electrolyte Solutions

Electrolyte 0.5 M	*Electroactive Area (cm^{-2})*[*]	*Onset of Oxidation (V)*	*M of Oxide Species ($gmol^{-1}$)*[†]	*Amount of Oxide (ng)*[‡]	*Monolayers of Oxide (ML)*
H_2SO_4	0.270	0.300	16.2	8.00	1.14
$HClO_4$	0.255	0.150	16.3	12.0	1.70
H_3PO_4	0.240	0.340		7.00	

3.4 Effect of H_2SO_4, $HClO_4$, and H_3PO_4 on Ag UPD at Pt EQCM

3.4.1 Results

Figure 3-4 (A) shows the CV scan for a Pt EQCM obtained in a solution of 0.5 mM $AgNO_3$ dissolved in 0.5 M aqueous H_2SO_4 electrolyte. The CV scans started at 0.310 V vs. MSE, which is the open circuit potential of the Pt EQCM in this silver containing solution, and only two complete CV scans where collected in order to observe the anodic features of interest and due to the structural changes occurring at the interface with further cycling in this solution that are beyond the scope of this study. The final potential of the scans was the same as the initial potential (OCP).

In the first cathodic scan the silver-under-potential deposition (UPD) is visually identified in the potential range of 0.300 V to 0 V and it is assumed that the peak corresponds only to the Ag UPD reaction since the Pt EQCM has been

---

[*] Electroactive area corresponding to mass sensing area only.

[†] From equation (5) $M = \frac{\delta \Delta mnF}{\Delta q}$

[‡] From individual mass-responses.

electrochemically cleaned, and the scan started at OCP where little or no PtO has been produced. The scan continues to reach a switch potential of -0.640 V in order to allow monitoring the complete Ag over-potential deposition (OPD).

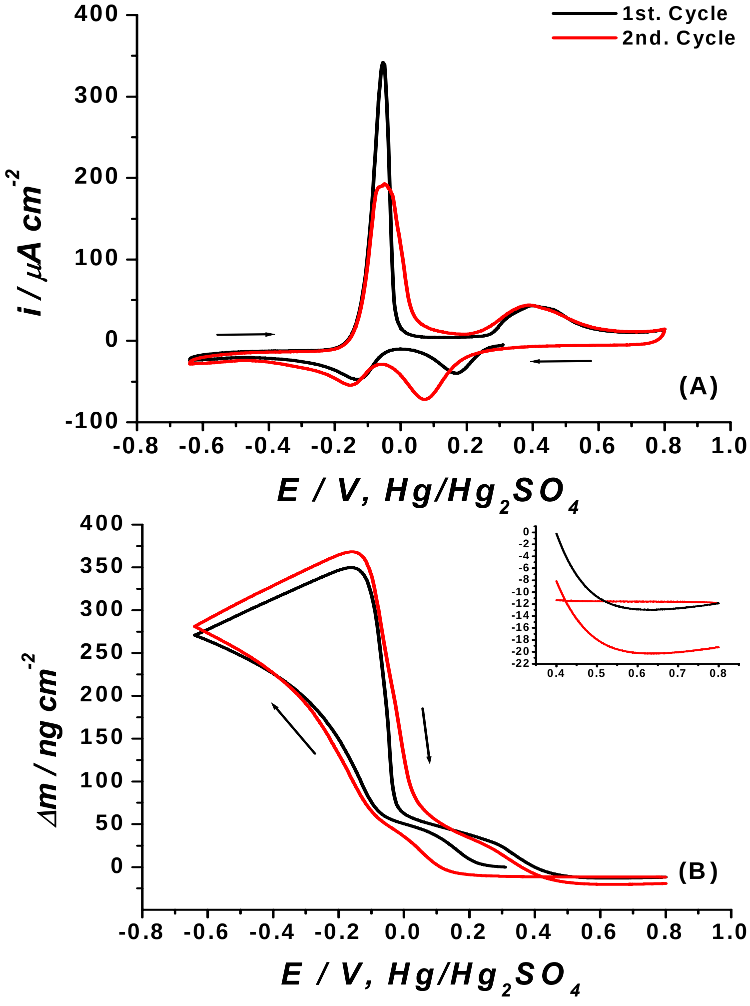

Figure 3-4 CV profile (A) and mass-response (B) for a Pt EQCM in 0.5 mM $AgNO_3$ / 0.5 M aqueous H_2SO_4.

In the reverse scan the Ag OPD stripping peak is observed between -0.150 V and 0 V with a peak potential (E_{Bulk}) at -0.0540 V. The Ag UPD stripping peak is observed between 0.200 V and 0.700 V, with a E_{UPD} at 0.300 V, and it is expected that the peak includes the charge contributions from the PtO formation, since both reactions are occurring in the same potential range. In a subsequent cathodic scan, the peaks corresponding to Ag UPD and PtO reduction are merged in the potential range of 0.300 V to -0.0500 V; in this scan, the resulting reduction peak is broader and expands to more negative potentials. Due to both reactions, the expected switching of potentials is observed. In the reverse scan the Ag OPD stripping is observed at E_{Bulk} = -0.0490 V, which is a little more positive than the E_{Bulk} of the first CV scan. The Ag UPD stripping and PtO deposition peak is found at E_{UPD} = 0.280 V, which switched a little towards negative potentials if compared to E_{UPD} from the first CV scan.

Figure 3-4 (B) shows the corresponding mass-response for the CV scans in Figure 3-4 (A), where it is possible to confirm the aforementioned regions by identifying the corresponding mass changes. In the initial cathodic scan, a light mass increase accompanies the potential region of 0.300 V to 0 V that has been identified as Ag UPD. Following towards more negative potentials, a dramatic mass increase is observed that corresponds to the Ag OPD, and that continues to the anodic scan until reaching the onset of Ag OPD stripping at -0.150 V, where a dramatic mass decrease is observed that corresponds to Ag OPD stripping. A less pronounced mass decrease is observed in the potential region corresponding to the Ag UPD stripping and the platinum oxidation reactions, and from the insert in Figure 3-4 (B) it is observed that there is indeed a light mass increase between 0.600 V and 0.800 V that can be exactly associated with PtO formation. In a similar manner the mass changes are observed for the second CV scan with some variations that will be discussed in further detail in section 3.4.2.

Figure 3-5 (A) shows the CV scan for a Pt EQCM obtained in a solution of 0.5 mM $AgNO_3$ dissolved in 0.5 M aqueous $HClO_4$ electrolyte. The CV scans started at 0.280 V vs. MSE, which is the open circuit potential of the Pt EQCM in the aforementioned solution, and only two complete CV scans where collected in order to observe the features of interest. The final potential of the scans was the same as the initial potential (OCP).

In the first cathodic scan the Ag UPD is identified in the potential region of 0.280 V to 0 V, and the onset of the Ag OPD bulk over-layers is found at -0.0500 V; the scan continues to reach a switch potential of -0.640 V in order to allow monitoring the complete Ag OPD.

In the reverse scan the Ag OPD stripping peak is observed between -0.150 V and 0.0500 V with E_{Bulk} = -0.0400 V. The Ag UPD stripping peak is observed between 0.200 V and 0.700 V, with a E_{UPD} = 0.300 V, and it is expected that the peak includes the charge contributions from the PtO formation, just like in H_2SO_4 solution. In the second CV scan, the cathodic peak corresponding to Ag UPD and PtO reduction is visually identified in the potential range of 0.250 V to -0.0550 V, integrating the charge density for the combination of reactions.

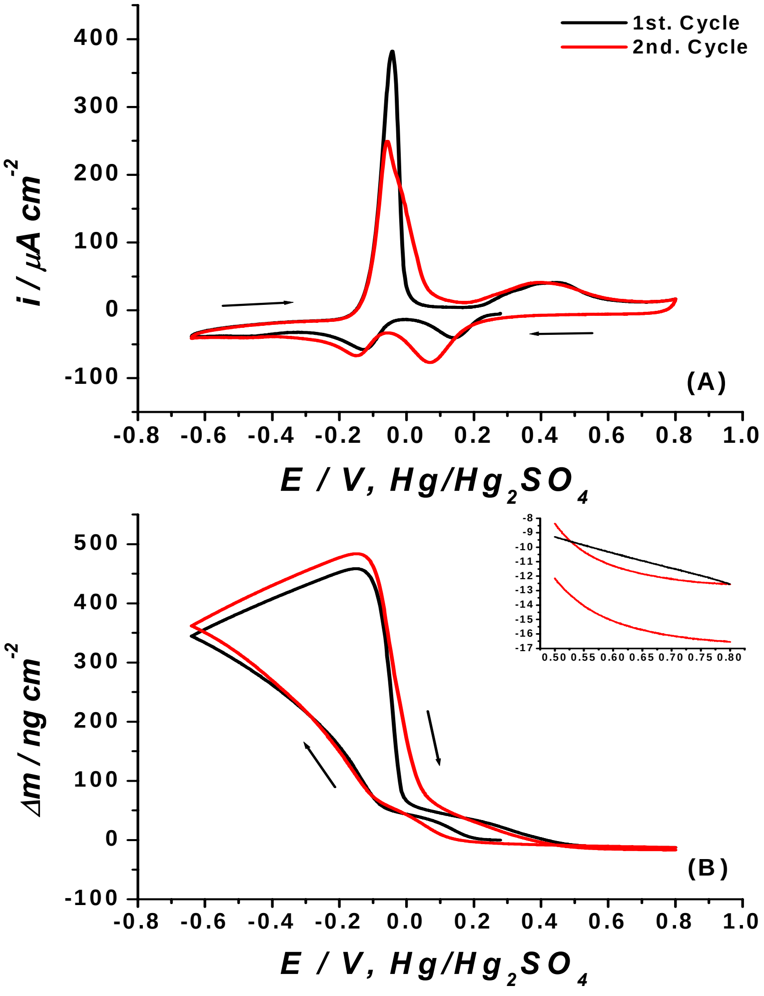

Figure 3-5 CV profile (A) and mass-response (B) for a Pt EQCM in

0.5 mM $AgNO_3$ / 0.5 M aqueous $HClO_4$.

In the reverse scan the Ag OPD stripping is observed at E_{Bulk} = -0.0580 V, which is a little more negative than the E_{Bulk} of the first CV scan. The Ag UPD stripping and PtO deposition peak is found at E_{UPD} = 0.270 V, which switched a little towards negative potentials if compared to E_{UPD} from the first CV scan.

Figure 3-5 (B) shows the corresponding mass-response for the CV scans in Figure 3-5 (A), where the mass changes corresponding to the aforementioned regions are identified. In the initial cathodic scan, a light mass increase accompanies the potential region of 0.280 V to 0 V that is identified as Ag UPD. Following towards more negative potentials, a dramatic mass increase is observed that corresponds to the Ag OPD, and that continues to the anodic scan until reaching the onset of Ag OPD stripping at -0.150 V, where a dramatic mass decrease is observed that corresponds to Ag OPD stripping. A less pronounced mass decrease is observed in the potential region for the Ag UPD stripping and the platinum oxidation reactions, and from the insert in Figure 3-5 (B) it is observed that there is no mass increase associated for PtO formation in this electrolyte as observed in H_2SO_4. In a similar manner the mass changes are observed for the second CV scan and these will be discussed in further detail in section 3.4.2.

Figure 3-6 (A) shows the CV scan for a Pt EQCM obtained in a solution of 0.5 mM $AgNO_3$ dissolved in 0.5 M aqueous H_3PO_4 electrolyte. The CV scans started at the OCP value of 0.280 V for the phosphoric acid electrolyte and two complete CV scans where collected. In the same manner, the final potential of the scans was the same as the initial potential (OCP).

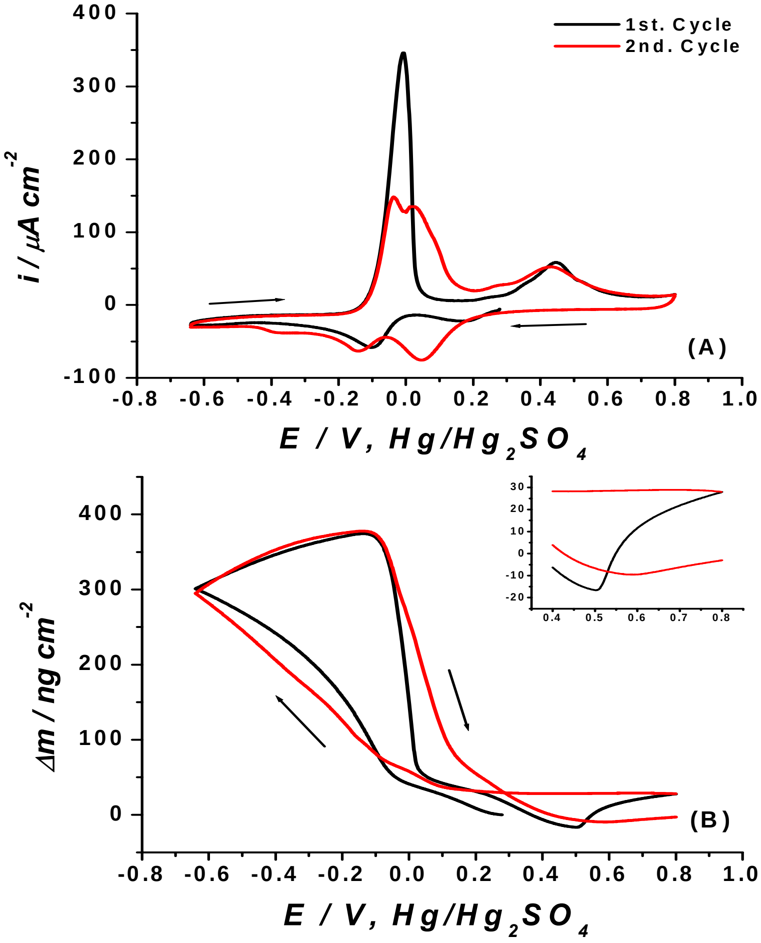

Figure 3-6 CV profile (A) and mass-response (B) for a Pt EQCM in 0.5mM $AgNO_3$ / 0.5M aqueous H_3PO_4.

In the first cathodic scan the Ag UPD is identified in the potential region of 0.280 V to 0.0250 V; the onset of the over-potential deposition (OPD) of Ag bulk over-layers is found at 0.0200 V, and the scan continues to reach a switch potential of -0.640 V to allow monitoring the complete Ag OPD. In the reverse scan the Ag OPD stripping peak is observed between -0.120 V and 0.0500 V with E_{Bulk} = -0.008 V. The Ag UPD stripping peak is observed between 0.200 V and 0.700 V, with a E_{UPD} = 0.270 V, and it is expected that the peak includes the charge contributions from the PtO formation, just like in the previous cases.

In the second CV scan, the cathodic peak corresponding to Ag UPD and PtO reduction is found in the potential range of 0.280 V to -0.060 V, integrating the charge density for the combination of reactions. The onset of Ag OPD is switched to more negative potentials as compared with the first cathodic scan, and in the reverse scan the Ag OPD stripping is observed at E_{Bulk} = -0.0360 V, which is more negative than the E_{Bulk} of the first CV scan. The Ag UPD stripping and PtO deposition peak is found at E_{UPD} = 0.270 V, which is lightly switched towards negative potentials if compared to E_{UPD} from the first CV scan.

Figure 3-6 (B) shows the corresponding mass-response for the CV scans in Figure 3-6 (A), and in the initial cathodic scan a mass increase accompanies the potential region of 0.280 V to 0.0250 V that could be identified as Ag UPD, and that will be discussed in more detail in the following sections. Towards more negative potentials, a dramatic mass increase is observed that corresponds to the Ag OPD, and that continues to the anodic scan until reaching the onset of Ag OPD stripping at -0.120 V, where a dramatic mass decrease is observed that corresponds to Ag OPD stripping. A less pronounced mass decrease is observed in the potential region for the Ag UPD stripping, and from the insert in Figure 3-7 (B) it is observed that there is a mass increase at 0.500 V that is identified as AgO produced by a reaction of the premonolayer oxidation or “active oxide” species, as will be described in the following section. In a similar manner the mass changes are observed for the second CV scan where changes on the kind of species adsorbed on the surface of the Pt EQCM modify the mass change related to the potential region shown in the insert of Figure 3-7 (B); these will be discussed in further detail in section 3.4.2.

3.4.2 Discussions

The cyclic voltammograms shown in Figures 3-5 (A), 3-6 (A) and 3-7 (A) are in close agreement with results previously published by Salvarezza et al [9], Martins et al [11], and Jeffrey et al [16]. The features in the voltammograms are observed by these authors at 1 mM and 0.5 mM silver concentrations in either 1 mM or 0.5 mM electrolyte concentrations, and the reversible reaction associated with the Ag UPD corresponds to:

$$Pt + Ag^{+} + e \Leftrightarrow PtAg_{(ads)} \qquad (7)$$

It is well known that this reaction occurs in the same potential region corresponding to the electro-reduction and oxidation of platinum, for which the reaction is:

$$PtO_{(s)} + 2e^- + 2H^+ \Leftrightarrow Pt + H_2O \tag{8}$$

And therefore the overall reaction occurring in this potential region can be written in the following manner:

$$PtO_{(s)} + Ag^+ + 2H^+ + 3e^- \Leftrightarrow H_2O + PtAg_{(ads)} \tag{9}$$

3.4.2.1 Thermodynamic parameters of Ag UPD on Pt EQCM

The change in free energy between under-potentially deposited silver and its platinum substrate can be calculated from equation (10) previously described in section 1.2 [38].

$$\Delta G = nF\Delta E_p \tag{10}$$

Where ΔE_p is the potential difference between OPD and UPD anodic peaks, n is the number of electrons transferred (1 electron transfer reaction in this case), and F is Faraday's constant. The larger value of ΔG° is an indication of the stronger binding energy between silver and platinum, as compared to silver deposited into its own lattice (Ag OPD). Therefore, in order to determine which electrolyte favors the stronger binding of Ag to the Pt EQCM, the change in free energy for both CV scans in each electrolyte were calculated, and results are shown in Table 3-2.

Table 3-2 Thermodynamic Parameters of Ag UPD on Pt EQCM

0.5 mM AgNO3 / 0.5 M Electrolyte	*CV scan*	E_{Bulk}	E_{UPD}	ΔE_p / V	ΔG / kJ/mol
H_2SO_4	1	-0.0540	0.300	0.354	34.2
	2	-0.0500	0.280	0.330	31.8
$HClO_4$	1	-0.0430	0.300	0.343	33.1
	2	-0.0580	0.270	0.328	31.7
H_3PO_4	1	-0.008	0.270	0.278	26.8
	2	-0.0360	0.270	0.306	29.5

It is observed that the stronger binding is for the first CV scan of Ag UPD from 0.5 M H_2SO_4 electrolyte, which has a ΔE_p = 0.354 V and a change in free energy of 34.2 kJ·mol^{-1}. For the second CV cycle in that same electrolyte the ΔG° values decreases to 31.8 kJ·mol^{-1}, as it is expected since the first UPD monolayer is always more favored than the subsequent ones. This holds true for Ag UPD from 0.5 M $HClO_4$ where the ΔG° = 33.1 kJ·mol^{-1} for the first CV scan, and it decreases slightly to ΔG° = 31.7 kJ·mol^{-1} for the second CV scan.

The case of Ag UPD from 0.5 M H_3PO_4 is different from sulfuric and perchloric acid since the first Ag UPD monolayer has a lower change in free energy than the second one, which is opposite to what we expected. It is possible that assumption of the existence of the premonolayer oxidation species [23] is playing an important role in the Ag UPD adsorption, and in the first CV scan there is more influence from these “active oxide” species that inhibit the reduction of Ag or the Ag UPD [39]. From literature it is know that these species form at potentials more negative than the platinum electro-oxidation (reason is why is called a premonolayer oxidation process) and is possible that these “active oxide” species can be formed at the open circuit potential (0.280 V) that was used as initial potential in the presented CV scan therefore inhibiting the strong binding of the first Ag UPD monolayer to the Pt surface. A change in the species present on the surface of the Pt EQCM may occur after completion of the first CV scan in H_3PO_4 that allow for the second Ag UPD monolayer to have a stronger binding energy to the Pt substrate.

Since it is known from literature that these premonolayer oxidation species are very active and promote oxidation of reactive species and organics like methanol and CO_{ads} [34, 40], there must be some reaction involved with the Ag in solution that produces silver oxide, therefore reducing the amount of “active species” in the second CV scan that allows a better binding of the second Ag UPD to the Pt substrate. These assumptions are supported by discussions in section 3.4.2.3.

3.4.2.2 Estimated Ag UPD Amounts from Sulfuric and Perchloric Acid Electrolytes from EQCM Mass-responses

The EQCM is a very powerful analytical instrument to elucidate chemical mechanisms and reactions occurring at the electroactive surface that could not be easily explained only by means of cyclic voltammetry, chronoamperometry, or any other electrochemical technique by itself. In combination with these techniques the EQCM's mass-responses acquired, allow for a better understanding of electrochemical systems where more than one well known electrochemical process is occurring at the electrode's surface.

The silver under-potential deposition on platinum from electrolyte solutions that favor the oxidation of platinum is a complex system to analyze, and with the EQCM's mass-responses the approximate nanograms corresponding to Ag UPD, Pt electro-oxidation, and any other reaction happening at the same time, can be obtained from the changes in mass occurring at the corresponding potential regions. These mass values can then be converted to monolayers and charge densities by very simple mathematical correlations.

For Ag UPD on Pt EQCM from sulfuric and perchloric acid solutions, it is more straight forward to identify the kinds of species that are present on top of the Pt surface, since it is well known that the two main reactions occurring at the selected potential region are that of Ag UPD and Pt oxidation. The system becomes somehow more complex to analyze when the electrolyte is changed for phosphoric acid due to interaction of "active oxide" species, the inability to identify the monolayer oxide species through equation (5), and the observation of relatively large changes in mass occurring at the anodic region that may account for oxidation of any of the species in solution, mainly Ag.

From Figure 3-4 (B), the change in mass associated with the Ag UPD stripping from H_2SO_4 solution in the potential region of 0.2 V to 0.7V is measured as Δm_{Ag} = 55.5 ng. In order to obtain the Ag UPD as monolayers of Ag from this mass-measurement, it is necessary to know the mass per Ag monolayer for the specified electroactive area. The following equation can be used to calculate the nanograms per monolayer corresponding to Ag or any other element or compound:

$$m_{iML} = 1.66x10^{-9}\frac{mol}{cm^2}\cdot A\cdot M \tag{11}$$

Where m_{iML} are the nanograms per monolayer of element *i*, $1.66x10^{-9}\frac{mol}{cm^2}$ is a constant resulting from Avogadro's number and the number of atoms per cm^2 for this system $\left[\left(\frac{1\times10^{15}\,\text{atoms}}{\text{cm}^2}\right)\left(\frac{\text{mol}}{6.02\times10^{23}\,\text{atoms}}\right)\right]$, *A* is the electroactive area, and *M* is the molar mass of the element or compound adsorbed on the surface. It is then calculated that one Ag monolayer corresponds to m_{AgML} = 48.0 and m_{AgML} = 46.0 nanograms for the sulfuric and perchloric acid environments respectively, and one O monolayer is m_{OML} = 7.00 ng for both electrolytes (knowing from section 3.2.2 that the oxide species correspond to PtO in these cases). Therefore the monolayers corresponding to Ag UPD are calculated from the mass-response by:

$$ML_{Ag} = \frac{\Delta m_{Ag}}{m_{AgML}} \tag{12}$$

And for sulfuric acid a mass decrease of Δm_{Ag} = 55.5 ng corresponds to 1.16 ML_{Ag} that are stripped off the surface. In a similar manner the number of monolayers for Ag UPD in perchloric acid are calculated by measuring a mass decrease of Δm_{Ag} = 50.5 ng observed in the potential region of 0.200 V and 0.700 V in the first anodic scan from Figure 3-5 (B), and the Ag UPD monolayers correspond to 1.10 ML_{Ag} taking into account that one silver monolayer is equivalent to m_{Ag} = 46.0 ng in perchloric acid.

Since Ag UPD stripping is occurring while PtO is formed on the surface, there exists a change in mass that has not been taken into account when calculating ML_{Ag} for these two systems. The ignored change in mass comes from the active sites that are immediately occupied by oxygen species after silver has left any site vacant, and even if the replacing oxygen species are much smaller than the laving silver atoms, it is possible to assume from the corresponding molar masses that close to 14% $\left(\frac{15.9\text{g/mol}}{108\text{g/mol}}\right)$ of the total amount of ML_{Ag} is ignored in the calculated results. In order to avoid this error, the values for Ag UPD were recalculated taking into account the change in mass of the sites that are immediately occupied by oxygen. Then, if it is known for H_2SO_4 that 1.16 ML_{Ag} corresponds to the 86.0 % of Ag UPD stripped off, then the total Ag UPD would correspond to approximately 1.34 ML_{Ag}. For $HClO_4$ is known that 1.10 ML_{Ag} correspond to the 86.0 % of Ag UPD stripped off, and then the total Ag UPD corresponds to approximately 1.27 ML_{Ag}.

The charge density contribution from the Ag UPD can then be obtained from the silver monolayers by the following correlation:

$$q_i = 1.60x10^{-4}\,\frac{C}{cm^2}\cdot ML_i \qquad (13)$$

Where 1.60x10^{-4} C·cm^2 is a constant for a one electron transfer reaction that comes from Faraday's constant, Avogadro's number, and the number of atoms per cm^2 $\left[\left(\frac{9.65x10^4\,C}{mol}\right)\left(\frac{1\times10^{15}\,atoms}{cm^2}\right)\left(\frac{mol}{6.02\times10^{23}\,atoms}\right)\right]$. Therefore, the charge density corresponds to q_{Ag} = 2.14 x10^{-4} C·cm^2 and q_{Ag} = 2.03 x10^{-4} C·cm^2 for the Ag UPD from sulfuric and perchloric acids respectively.

Table 3-3 Ag UPD Calculations for H_2SO_4 and $HClO_4$

	0.5mM $AgNO_3$ / 0.5 M H_2SO_4	*0.5mM $AgNO_3$ / 0.5 M $HClO_4$*
q_{Ag} ($x10^{-4}$ $C\cdot cm^2$)	2.14	2.03
ML_{Ag}	1.34	1.27
Δm_{Ag} ($x10^{-9}$ g)	64.3	58.4

Table 3-3 summarizes the calculated amounts for Ag UPD from sulfuric and perchloric acid electrolytes in charge densities, change in mass, and number of monolayers after taking into account the change in mass corresponding to the

Ag UPD sites that are immediately occupied by oxygen atoms after they are left vacant

3.4.2.3 Estimated Ag UPD Amounts from Phosphoric Acid Electrolyte and the Effect of the Pt Premonolayer Oxidation

Figure 3-6 (B) shows a light mass decrease in the potential region of 0.200 V to 0.500 V that corresponds to Δm_{Ag} = 51.1 ng of Ag UPD desorption, and that is followed by a relatively large increase in mass from 0.500 V to 0.800 V that corresponds to an unknown kind of oxidized species which may include some contributions from PtO formation. By means of equation (11) is known that one silver monolayer in this case corresponds to m_{AgML} = 43.0 ng, and with equation (12) is calculated that the measured Δm_{Ag} = 51.1 ng of Ag UPD corresponds to 1.20 ML_{Ag}; with equation (13) the charge associated with this calculated value is 1.90 x10^{-4} C·cm^{-2}.

From section 3.4.2 and reference [23] is known that the platinum oxide species that grow on Pt EQCM when immersed in phosphoric acid cannot be elucidated by means of equation (5) due to the presence of “active oxide” species that differ of those on the anodic monolayer region. Since these “active oxide” species promote oxidation, it is possible that the mass increase observed in the insert of Figure 3-6 (B) corresponds to oxidized species that differ from PtO and that are a product of a reaction of the “active oxide” species with other ions in solution like Ag ions or perchlorate ions.

Therefore, in order to identify the species adsorbed on the Pt surface at the potential region of 0.500 V to 0.800 V, a plot of current density vs. mass density is made with the data points from this region.

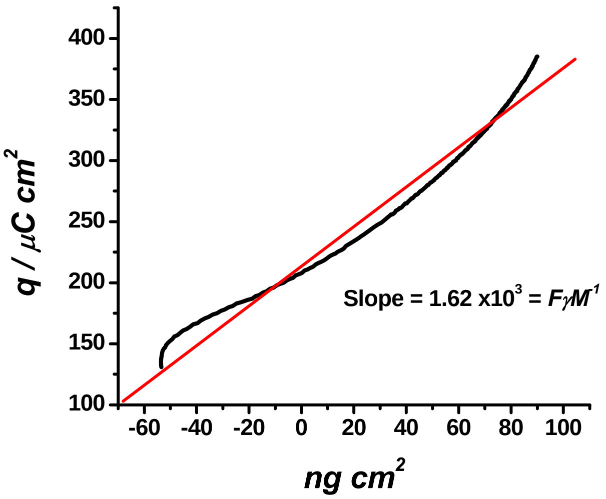

Figure 3-7 Charge density measurements vs. mass density for the deposition of oxidized species different from PtO.

Figure 3-7 show the resulting plot, where the slope of the linear fit corresponds to $\frac{F\gamma}{M}$ where F is the Faraday's constant, γ is the charge of the oxidized ion or adsorbed species, and M the molar mass of the adsorbed species. With the slope value of 1.62 $\times10^3$, the value for $\frac{\gamma}{M}$ once the quotient of the slope and the Faraday's constant is obtained is $\frac{\gamma}{M}$ = 0.0168. If the assumption is made that the species correspond to PtO, the value of $\frac{\gamma}{M}$ = 0.125; assuming that the "active oxide" species reacted with Ag ions in solution to produce AgO (M=124 g·mol^{-1}) with an oxidation state of +2 for Ag, then the value for $\frac{\gamma}{M}$ = 0.0162 which is close to the product of the slope and Faraday's constant ($0.0168 \approx 0.0162$).

Small deviation from the predicted value can be associated to a mixture of Ag_2O (where Ag ion is +1) and AgO, since it is known from literature that silver oxide films tend to grow in combination with Ag_2O as precursor of AgO when anodizing silver electrodes in concentrated sodium hydroxide solutions [41], and silver acetate and sodium acetate solutions [42]; but is evident the dominant or favored specie is AgO in the present work.

The production of silver oxides observed at Pt EQCM on phosphoric acid solutions is a direct evidence of existence of "active oxide" species or premonolayer oxidation species which are different to the expected PtO, and that are very reactive towards oxidation of surrounding species to an obvious extent.

From the insert in Figure 3-6 (B) the change in mass for the potential region of 0.500 V to 0.800 V corresponds to an increase of Δm_{AgO} = 44.4 ng that is equivalent to 0.750 ML_{AgO} or 2.04 x10^{-4} C·cm^{-2}. The total integrated charge density for the anodic peak that corresponds to Ag UPD stripping, AgO adsorption, and possible PtO formation corresponds to 4.28 x10^{-4} C·cm^{-2}; subtracting the charge density associated to Ag UPD stripping and AgO adsorption from the total charge density, results in 3.35 x10^{-5} C·cm^{-2} that can be associated to PtO, which corresponds to 0.210 ML_{PtO} or 1.30 ng of PtO.

Table 3-4 show the results for the Ag UPD, PtO, and AgO calculated amounts for the three different electrolytes.

Table 3-4 Ag UPD, PtO and AgO Calculations

	0.5mM $AgNO_3$ / 0.5 M H_2SO_4	*0.5mM $AgNO_3$ / 0.5 M $HClO_4$*	*0.5mM $AgNO_3$ / 0.5 M H_3PO_4*
q_{Ag} (x10^{-4} C·cm^2)	2.14	2.03	1.90
ML_{Ag}	1.34	1.27	1.18
Δm_{Ag} (x10^{-9} g)	64.3	58.4	51.1
q_{AgO} (x10^{-4} C·cm^2)			2.40
ML_{Ag}			0.750
Δm_{Ag} (x10^{-9} g)			44.4

The results show a slightly preferred Ag UPD when sulfuric acid is used as an electrolyte, but is clear that the amount of Ag UPD is preferentially close to one monolayer for the three electrolytes used under the conditions used in these experiments.

The observation of AgO growth on Pt EQCM when phosphoric acid is used as an electrolyte could be of significant importance for the recent fabrication of nitrate-sensing systems where silver oxide is used for coating electrodes inside the sensing device, and which require controlled amounts of AgO [43]. This is important because of the significant risk that nitrate represents to human health as a major contaminant in ground-water and surface-water systems. Additional uses for AgO are found as bactericides due to its activity for bactericidal treatment of water in medicine, or as device to reduce CO contents due to its reactivity towards this compound [44].

3.5 Conclusions

In this chapter, the EQCM was used to study the effect of sulfuric, perchloric and phosphoric acids on Ag UPD when used as electrolyte solutions. The results account for values close to one monolayer of Ag UPD deposited on Pt EQCM independently of the used electrolyte, being slightly larger when sulfuric acid is used. The PtO growth is favored by perchloric acid solution as observed from the mass-responses acquired for the background CV scans.

The EQCM proved to be such a powerful tool for analysis of CV data that involves several reactions in the same potential region, and that would have not been possible by pure cyclic voltammetry in this very straight forward manner. In presence of silver atoms and phosphoric acid, the EQCM allowed monitoring the reaction of low coverage “active oxide” species, and the identification of AgO as product of this reaction which has not been reported previously by literature. This can be of interest for fabrication of micro-sensing devices for the detection of contaminants, and for the production of AgO for its use as bactericidal.

3.6 References

1. Bruckenstein, S.; Shay, M., *Electrochim. Acta,* 1985. 30(10): p. 1295-1300.
2. Martin, B.A.; Hager, H.E., *J. App. Phy*s. 1989. 65(7): p. 2627-2629.
3. Bund, A.; Schwitzgebel, G., *Electrochim. Acta,* 2000. 45: p. 3703-3710.
4. Gileadi, E.; Tsionsky, V., *J. Electrochem. Soc.* 2000. 147(2): p. 567-574.
5. Tang, Y.; Furtak, T.E.; *Electrochim. Acta,* 1991. 36(11/12): p. 1873-1877.
6. Palomar-Pardavé, M.; González, I.; Batina, N., *J. Phys. Chem.* 2000. 104: p. 3545-3555.
7. Girija, T.C.; Sangaranarayanan, M.V., *J. Solid State Electrochem.* 2005. 9: p. 621-626.
8. Tindall, G.W.; Bruckenstein, S., *Electrochim. Acta,* 1971. 16: p. 245-253.
9. Salvarezza, R.C.; Vásquez Moll, D.V.; Giordano, M.C.; Arvia, A.J., *J. Electroanal. Chem.* 1986. 213: p. 301-312.
10. Parajón Costa, B.; Canullo, J.; Vásquez Moll, D.; Salvarezza, R.C.; Giordano, M.C.; Arvia, A.J., *J. Electroanal. Chem.* 1988. 244: p. 261-272.
11. Martins, M. E.; Salvarezza, R. C.; Arvia, A. J., *Electrochim.* Acta, 1991. 36(10): p. 1617-1622.
12. Mascaro, L. H.; Santon, M. C.; Machado, S. A. S.; Avaca, L. A.; *J. Chem. Soc. Faraday Transactions,* 1997. 93(22): p. 3999-4003.
13. Palacio, C.; Ocón, P.; Herrasti, P.; Díaz, D.; Arranz, A., *J. Electroanal. Chem.* 2003. 545: p. 53-58.

14. Attard, G.A.; Al-Akl, A.; *J. Electroanal. Chem.* 2003. 554-555: p. 439-448.
15. Iwata, F.; Saruta, K.; Sasaki, A.; *Appl. Phys. A,* 1998. 66: p. S463-S466.
16. Jeffrey, C.A.; Storr, W. M.; Harrington, D.A., *J. Electroanal. Chem.* 2004. 569: p. 61-70.
17. Watanabe, M.; Uchida, H.; Ikeda, N., *J. Electroanal. Chem.* 1995. 380: p. 255-260.
18. Jusys, Z.; Bruckenstein, S., *Electrochem. Communications,* 2000. 2: p. 412-416.
19. Santos, M.C.; Miwa, D.W.; Machado, S.A.S., *Electrochem. Communications,* 2000. 2: p. 692-296.
20. Jerkiewicz, G.; Vatankhah, G.; Lessard, J.; Soriaga, M.P.; Park, Y.-S., *Electrochim. Acta,* 2004. 49: p. 1451-1459.
21. Wieckowski, A.; Kolics, A., *J. Phys. Chem. B.* 2001. 105: p. 2588-2595.
22. You, H.; Zurawski, D. J.; Nagy, Z.; Yoncoa, R. M., *J. Chem. Phys.* 1994. 100 (6): p. 4699-4702.
23. Burke, L.D.; Morrissey, J.A., *J. Electrochem. Soc.*, 1994. 141(9): p. 2361-2368.
24. Conway, B.E., *Modern Aspects of Electrochemistry No.38*, 2005. New York: Kluwer Academic/Plenum Publishers. p. 375.
25. Wieckowski, A.; *Interfacial Electrochemistry: Theory, Experiment, and Applications*, 1999. New York: Marcel Dekker, Inc. p. 559.

26. Tremiliosi-Filho, G.; Jerkiewicz, G.; Conway, B.E., *Langmuir*, 1992. 8: p. 658-667.
27. Gamboa-Aldeco, M.E.; Herrero, E.; Zelenay, P.S.; Wieckovwski, A., *J. Electroanal. Chem.* 1993. 348: p. 451-457.
28. Biegler, T.; Woods, R., *Electroanal. Chem. Interfac. Electrochem.* 1968. 20: p. 73-78.
29. Hepel, M., *Electrode-Solution Interface Studied with Electrochemical Quartz Crystal Nanobalance*, in *Interfacial Electrochemistry*, ed, Wieckowski, A., 1999, Marcel Dekker: Potsdam. p. 599-629.
30. Lu, C., *Applications of Piezoelectric Quartz Crystal Microbalances*, in *Methods and Phenomena: Their application in Science and Technology*, Ed. Lu, C., 1984, Elsevier Science: Amsterdam. p. 393.
31. Campbell, D.J.; Corn, R.M., *J. Phys. Chem.* 1988. 92: p. 5796-5800.
32. Desilvestro, J.; Weaver, M.J., *J. Electroanal. Chem.* 1986. 209: p. 377.
33. Kuver, A.; Vielstich, W.; Kitzelmann, D., *J. Electroanal. Chem.* 1993. 353: p. 255.
34. Burke, L.D.; Healy, J.F.; O'Dwyer, K.J.; O'Learly, W.A., *J. Electrochem. Soc.*, 1989. 136: p. 1015.
35. Burke, L.D.; Cunnane, V.J., *J. Electrochem. Soc.* 1986. 133: p. 1657.
36. Uchida, H.; Hiei, M.; Watanabe, M., *J. Electroanal. Chem.* 1998. 452: p.97.
37. Sauerbrey, G., Zeitschrift fuer Physik, 1959. 155: p. 206-222.

38. Zhang, Y.; Huang, L.; Arunagiri, T. N.; Ojeda, O.; Flores, S.; Chyan, O., *Electrochem. Solid-State Letters*, 2004. 7(9): p. C107-C110.

39. Burke, L.D.; O'Sullivan; O'Dwyer, K.J.; Scannell, R.A.; Ahern, M.J.G.; McCarthy, M.M., *ibid.,* 1990. 137: p. 2476.

40. Kunimatsu, K.; Seki, H.; Golden, W.G.; Gordon, J.G.; Philopott, M.R., *Langmuir*, 1986. 2: p. 464.

41. Uk Hur, T.; Sub Chung, W., *J. Electrochem. Soc.*, 2005. 152(5): p. A996-A1000.

42. Breyfogle, B.E.; Hung, C.J.; Shumsky, M.G.; Switzer, J.A., *J. Electrochem. Soc.* 1996. 143(9): p. 2741-2746.

43. Kim, D.; Goldberg, I.B.; Judy, J.W. 2004.

44. Wokaun, A.; Kötz, R.; Scherer, G.G.; Raimondi, F., *Angew. Chem. Int. Ed.*, 2005. 44: p. 2190-2209.

REFERENCE LIST

1. Gerisher, H.; Kolb, D.M.; Przasnyski, M.; *Surface Science* 1974, 43, 662-666.
2. Kolb, D.M., *Advances in Electrochemistry and Electrochemical Engineering,* 1978. John Wiley Interscience: New York. vol. 11. p. 125.
3. Kolb, D.M.; Przasnyski, M.; Gerisher, H.; *Electroanal. Chem. Interfac. Electrochem.* 1974, 54, 25-38.
4. Swathirajan, S.; Bruckenstein, S.; *Electrochim. Acta* 1983, 28(7), 865-877.
5. Van Huong C.N.; Gonzalez-Tejera, M.J.; *J. Electroanal. Chem.* 1988 244, 249-259.
6. Herrero, E.; Buller, L.J.; Abruña, H.D.; *Chem. Rev.* 2001, 101, 1897-1930.
7. Faulkner, L.R. Electrochemical *Characterization of Chemical Systems*. 1983. Academic Press, Inc.: vol. 3. p. 137.
8. Grosser, D.K., *Cyclic Voltammetry: Simulation and Analysis of Reaction Mechanism*. 1993, New York: Wiley-VCH.
9. Buttry D. A.; Ward, M. D. *Chem. Review,* 1992, *92,* 1355-1379.
10. Zhang, M., Ph. D. Thesis, University of Ottawa: Ottawa, Canada, 1995.
11. Salt, D. *Hy-Q Handbook of Quartz Crystal Devices,* Van Nostrand Reinhold: UK, 1987, pp 5-36, 160-162.

12. Buttry, D.A. *Applications of the Quartz Crystal Microbalance to Electrochemistry*, in *Electroanalytical Chemistry: A series of Advances*; Bard, A. J. Marcel Dekker: New York, 1996, pp 1-85.
13. Bard, A. J.; Faulkner, L. R. *Electrochemical Methods: Fundamentals and Applications*. Second Edition, John Wiley and Sons Inc.: New York, 2001, pp 725.
14. Aurbach, D.; Moshkovich, M. *J. Electrochem. Soc.* 1998, 145(8), 2629-2639.
15. Il-Hwan, K.; Kwang-Bum, K. *J. Electrochem. Soc.* 2004, 151(1), E7-E13.
16. Ostrom, G. S.; Buttry, D. A. *J. Phys. Chem.* 1995, 99(41), 15236-40.
17. Ariizumi, N.; Kamijo, M. *Yamanashi-ken Kogyo Gijutsu Senta Kenkyu Hokoku* 2000, 14, 12-17.
18. Sadik, O. A.; Cheung, M-C. *Talanta* 2001, 55(5), 929-941.
19. O’Sullivan, C.K.; Guilbault, G. G. *Biosensors & Bioelectronics* 1999, 14, 663-670.
20. Lee, W.; White, H. S.; Ward, M. D. *Anal. Chem.* 1993, 65, 3232-3237.
21. Deakin, M.R.; Buttry, D. A. *Anal. Chem.* 1989, 61(20), 1147A-1154A.
22. Wunsche, M. *Electrochim. Acta* 1995, 5(40), 629-635.
23. Kraznaric, G. *Langmuir* 2001, 17, 43-4351.
24. Lay et al. *J. Electroanal. Chem.* 2003, 1, 1-11.

25. Herrero, E.; Buller, L. J.; Abruña, H. D. *Chem. Rev.* 2001, 101(7), 1897-1930.

26. Nicic, L. et al. *J. Phys. Chem. B* 2002, 106, 12247-12252.

27. Uchida, H.; Hiei, M.; Watanabe, M. *J. Electroanal. Chem.* 1998, 452(1), 97-106.

28. Marx, K.A., et al. *Biosensors and Bioelectronics* 2001, 16, 773-782.

29. Tenreiro, A.; Cordas, C. M.; Abrantes, L. M. *Portugaliae Electrochim. Acta* 2003, 21(4), 361-370.

30. Jiang, M.; Ray, W. W.; Mukherjee, B.; Wang, J. *Electrochem. Comm.* 2004, 6, 576-582.

31. Ward, M.D.; Buttry, D.A.; *Science*, 1990, 249(4972), 1000-1007.

32. Deakin, M.R.; Buttry, D.A.; *Anal. Chem*. 1989, 61(20), 1147A-1154A.

33. Jeffrey, M.I.; Zheng, J.; Ritchie, I.M.; *Meas. Sci. Technol*. 2002, 11, 560-567.

34. Vergé, M.-G.; Mettraux, P.; C.-O.A.Olsson,; Landolt, D.; *J. Electroanal. Chem.* 2004, 566, 361-370.

35. Cliffel, D.E.; Bard, A.J.; *Anal. Chem*. 1998, 70, 1993-1998.

36. Mecea, V.M.; Sensors and Actuators A, 2006, 128, 270-277.

37. Nascente, P.A.P., *Journal of Molecular Catalysis A: Chemical*, 2005. 228: p. 145-150.

38. Flores, S. *Making an Electrode*, 2003.

39. Gerisher, H.; Kolb, D.M.; Przasnyski, M.; *Surface Science* 1974, 43, 662-666.

40. Kolb, D.M., *Advances in Electrochemistry and Electrochemical Engineering,* 1978. John Wiley Interscience: New York. vol. 11. p. 125.

41. Kolb, D.M.; Przasnyski, M.; Gerisher, H.; *Electroanal. Chem. Interfac. Electrochem.* 1974, 54, 25-38.

42. Swathirajan, S.; Bruckenstein, S.; *Electrochim. Acta* 1983, 28(7), 865-877.

43. Van Huong C.N.; Gonzalez-Tejera, M.J.; *J. Electroanal. Chem.* 1988 244, 249-259.

44. Herrero, E.; Buller, L.J.; Abruña, H.D.; *Chem. Rev.* 2001, 101, 1897-1930.

45. Zhang, Y.; Huang, L.; Arunagiri, T. N.; Ojeda, O.; Flores, S.; Chyan, O., *Electrochem. Solid-State Letters*, 2004. 7(9): p. C107-C110.

46. Chyan, O.; Arunagiri, T.N.; Ponnuswamy, T., *J. Electrochem. Soc.* 2003. 150: p. C347.

47. Chan, R., *Interfacial Electrochemistry and Surface Characterization: Hydrogen Terminated Silicon, Electrolessly Deposited Palladium & Platinum on Pyrolyzed Photoresist Films and Electrodeposited Copper on Iridium*. 2003.

48. Jingying, S.; Xuifeng, Xiao; Zeshan, Z.; Xi, Z., *Dianhuaxue*, 1998. 4(2): p. 159-163.

49. Ureta-Zanartu, S.M..; Bravo, P.; Zagal, J.H., *J. Electroanal. Chem.* 1992. 337(1-2): p. 241-51.

50. Josell, D.; Bonevich, J.E.; Moffat, T.P.; Aaltonen, T.; Ritala, M.; Leskelä, M., *Electrochem. Solid-State Letters,* 2006. 9(2): p. C48-C50.

51. Pickup, P.G.; Birss, V.I., *J. Electroanal. Chem.* 1987. 220: p. 83-100.

52. Wagner, C.D., *Handbook of X-Ray Spectroscopy*.

53. Ojeda Mota, O.U., *Interfacial Study of Copper Electrodeposition with the Electrochemical Quartz Crystal Microbalance (EQCM).* 2005.

54. Zhang, Y., Dissertation. 2005.

55. Grujicic, D. and Pesic, B., *Electrochemica Acta*, 2002. 47(18): p. 2901-2912.

56. Hoare, J.P., J. Electroanal. Chem. 1968. 18: p. 251-259.

57. Conway, B.E.; Mozota, J., Electrochim. Acta, 1983. 28(1): p. 9-16.

58. Conway, B.E.; Mozota, J., Electrochim. Acta, 1983. 28(1): p. 1-8.

59. Fitzgerald, K.P.; Nairn, J.; Atrens, A., *Corr. Sci.* 1998. 40(12): p. 2029-2050.

60. Jouen, S.J.,and Hannoyer,B ., *Surface and Interface Analysis*, 2000. 30: p. 145-148.

61. Watanabe, M.; Tomita, M.; Ichino, T., *J. Electrochem. Soc.* 2001. 148(12): p. B522-B-528.

62. Barthelmy, D., *http://webmineral.com/data/Posnjakite.html.* 2004.

63. Helliwell, M. and Smith, J.V., *Acta Crystallographica, Section C.*, 1997. C53: p. 1369-1371.

64. Danilov, A.I.; Polukarov, Yu.M.; Climent, J. M.; Feliu, J. M., *Electrochim. Acta*, 2001. 46: p. 3137-3145.

65. Zerbino, J.O, *Journal of Applied Electrochemistry*, 1997. 27: p. 335-344.

66. Cascalheira, A.C. and Abrantes, M.L., *Electrochimica Acta*, 2004. 49: p. 5023-5028.

67. Christy, A.G., et al., *Journal of Applied Electrochemistry*, 2004. 34: p. 225-233.

68. Rand, D.A.J.; Woods, R., *J. Electroanal. Chem.* 1974. 55: p. 375-381.

69. Stonehart, P.; Angerstein-Kozlowska, H.; Conway, B.E., *Proc. R. Soc. Lond.* 1969. 541: p. A310.

70. Woods, R., *J. Electroanal. Chem.* 1974. 49: p. 217.

71. Sherwood, P.M.A., *Surface Science*. 1980. 101: p. 619-623.

72. Bruckenstein, S.; Shay, M., *Electrochim. Acta,* 1985. 30(10): p. 1295-1300.

73. Martin, B.A.; Hager, H.E., *J. App. Phy*s. 1989. 65(7): p. 2627-2629.

74. Bund, A.; Schwitzgebel, G., *Electrochim. Acta,* 2000. 45: p. 3703-3710.

75. Gileadi, E.; Tsionsky, V., *J. Electrochem. Soc.* 2000. 147(2): p. 567-574.

76. Tang, Y.; Furtak, T.E.; *Electrochim. Acta,* 1991. 36(11/12): p. 1873-1877.

77. Palomar-Pardavé, M.; González, I.; Batina, N., *J. Phys. Chem.* 2000. 104: p. 3545-3555.

78. Girija, T.C.; Sangaranarayanan, M.V., *J. Solid State Electrochem.* 2005. 9: p. 621-626.

79. Tindall, G.W.; Bruckenstein, S., *Electrochim. Acta,* 1971. 16: p. 245-253.

80. Salvarezza, R.C.; Vásquez Moll, D.V.; Giordano, M.C.; Arvia, A.J., *J. Electroanal. Chem.* 1986. 213: p. 301-312.

81. Parajón Costa, B.; Canullo, J.; Vásquez Moll, D.; Salvarezza, R.C.; Giordano, M.C.; Arvia, A.J., *J. Electroanal. Chem.* 1988. 244: p. 261-272.

82. Martins, M. E.; Salvarezza, R. C.; Arvia, A. J., *Electrochim.* Acta, 1991. 36(10): p. 1617-1622.

83. Mascaro, L. H.; Santon, M. C.; Machado, S. A. S.; Avaca, L. A.; *J. Chem. Soc. Faraday Transactions,* 1997. 93(22): p. 3999-4003.

84. Palacio, C.; Ocón, P.; Herrasti, P.; Díaz, D.; Arranz, A., *J. Electroanal. Chem.* 2003. 545: p. 53-58.

85. Attard, G.A.; Al-Akl, A.; *J. Electroanal. Chem.* 2003. 554-555: p. 439-448.

86. Iwata, F.; Saruta, K.; Sasaki, A.; *Appl. Phys. A,* 1998. 66: p. S463-S466.

87. Jeffrey, C.A.; Storr, W. M.; Harrington, D.A., *J. Electroanal. Chem.* 2004. 569: p. 61-70.

88. Watanabe, M.; Uchida, H.; Ikeda, N., *J. Electroanal. Chem.* 1995. 380: p. 255-260.

89. Jusys, Z.; Bruckenstein, S., *Electrochem. Communications,* 2000. 2: p. 412-416.

90. Santos, M.C.; Miwa, D.W.; Machado, S.A.S., *Electrochem. Communications,* 2000. 2: p. 692-296.

91. Jerkiewicz, G.; Vatankhah, G.; Lessard, J.; Soriaga, M.P.; Park, Y.-S., *Electrochim. Acta,* 2004. 49: p. 1451-1459.

92. Wieckowski, A.; Kolics, A., *J. Phys. Chem. B.* 2001. 105: p. 2588-2595.

93. You, H.; Zurawski, D. J.; Nagy, Z.; Yoncoa, R. M., *J. Chem. Phys.* 1994. 100 (6): p. 4699-4702.

94. Burke, L.D.; Morrissey, J.A., *J. Electrochem. Soc.*, 1994. 141(9): p. 2361-2368.

95. Conway, B.E., *Modern Aspects of Electrochemistry No.38*, 2005. New York: Kluwer Academic/Plenum Publishers. p. 375.

96. Wieckowski, A.; *Interfacial Electrochemistry: Theory, Experiment, and Applications*, 1999. New York: Marcel Dekker, Inc. p. 559.

97. Tremiliosi-Filho, G.; Jerkiewicz, G.; Conway, B.E., *Langmuir*, 1992. 8: p. 658-667.

98. Gamboa-Aldeco, M.E.; Herrero, E.; Zelenay, P.S.; Wieckovwski, A., *J. Electroanal. Chem.* 1993. 348: p. 451-457.

99. Biegler, T.; Woods, R., *Electroanal. Chem. Interfac. Electrochem.* 1968. 20: p. 73-78.

100. Hepel, M., *Electrode-Solution Interface Studied with Electrochemical Quartz Crystal Nanobalance*, in *Interfacial Electrochemistry*, ed, Wieckowski, A., 1999, Marcel Dekker: Potsdam. p. 599-629.

101. Lu, C., *Applications of Piezoelectric Quartz Crystal Microbalances*, in *Methods and Phenomena: Their application in Science and Technology*, Ed. Lu, C., 1984, Elsevier Science: Amsterdam. p. 393.

102. Campbell, D.J.; Corn, R.M., *J. Phys. Chem.* 1988. 92: p. 5796-5800.

103. Desilvestro, J.; Weaver, M.J., *J. Electroanal. Chem.* 1986. 209: p. 377.

104. Kuver, A.; Vielstich, W.; Kitzelmann, D., *J. Electroanal. Chem.* 1993. 353: p. 255.

105. Burke, L.D.; Healy, J.F.; O'Dwyer, K.J.; O'Learly, W.A., *J. Electrochem. Soc.*, 1989. 136: p. 1015.

106. Burke, L.D.; Cunnane, V.J., *J. Electrochem. Soc.* 1986. 133: p. 1657.

107. Uchida, H.; Hiei, M.; Watanabe, M., *J. Electroanal. Chem.* 1998. 452: p.97.

108. Sauerbrey, G., Zeitschrift fuer Physik, 1959. 155: p. 206-222.

109. Zhang, Y.; Huang, L.; Arunagiri, T. N.; Ojeda, O.; Flores, S.; Chyan, O., *Electrochem. Solid-State Letters*, 2004. 7(9): p. C107-C110.

110. Burke, L.D.; O'Sullivan; O'Dwyer, K.J.; Scannell, R.A.; Ahern, M.J.G.; McCarthy, M.M., *ibid.,* 1990. 137: p. 2476.

111. Kunimatsu, K.; Seki, H.; Golden, W.G.; Gordon, J.G.; Philopott, M.R., *Langmuir*, 1986. 2: p. 464.

112. Uk Hur, T.; Sub Chung, W., *J. Electrochem. Soc.*, 2005. 152(5): p. A996-A1000.

113. Breyfogle, B.E.; Hung, C.J.; Shumsky, M.G.; Switzer, J.A., *J. Electrochem. Soc.* 1996. 143(9): p. 2741-2746.

114. Kim, D.; Goldberg, I.B.; Judy, J.W. 2004.

115. Wokaun, A.; Kötz, R.; Scherer, G.G.; Raimondi, F., *Angew. Chem. Int. Ed.*, 2005. 44: p. 2190-2209.